

PHOTOMETRIC DETERMINATION OF THE MASS ACCRETION RATES OF PRE-MAIN SEQUENCE STARS. IV.  
RECENT STAR FORMATION IN NGC 602<sup>\*</sup>

GUIDO DE MARCHI,<sup>1</sup> GIACOMO BECCARI<sup>2</sup> AND NINO PANAGIA,<sup>3,4,5</sup>

(Received 11 April 2013; Accepted 28 July 2013)

ABSTRACT

We have studied the young stellar populations in NGC 602, in the Small Magellanic Cloud, using a novel method that we have developed to combine *Hubble Space Telescope* photometry in the  $V$ ,  $I$ , and  $H\alpha$  bands. We have identified about 300 pre-main sequence (PMS) stars, all of which are still undergoing active mass accretion, and have determined their physical parameters (effective temperature, luminosity, age, mass and mass accretion rate). Our analysis shows that star formation has been present in this field over the last 60 Myr. In addition, we can recognise at least two clear, distinct, and prominent episodes in the recent past: one about 2 Myr ago, but still ongoing in regions of higher nebulosity, and one (or more) older than 30 Myr, encompassing both stars dispersed in the field and two smaller clusters located about  $100''$  north of the centre of NGC 602. The relative locations of younger and older PMS stars do not imply a causal effect or triggering of one generation on the other. The strength of the two episodes appears to be comparable, but the episode occurring more than 30 Myr ago might have been even stronger than the current one. We have investigated the evolution of the mass accretion rate  $\dot{M}_{\text{acc}}$  as a function of the stellar parameters finding that  $\log \dot{M}_{\text{acc}} \simeq -0.6 \log t + \log m + c$ , where  $t$  is the age of the star,  $m$  its mass and  $c$  is a decreasing function of the metallicity.

*Subject headings:* stars: formation – stars: pre-main-sequence – Magellanic Clouds

1. INTRODUCTION

The young star cluster NGC 602 and the associated H II region N90 (Henize 1956) are located in a relatively isolated and diffuse environment in the “wing” of the Small Magellanic Cloud (SMC), towards the edge of the Magellanic Bridge. In many ways, NGC 602 represents an extragalactic analogue to the greater Orion OB association: it has a similar overall size ( $\sim 50$  pc), it contains similarly few O-type stars of about the same age ( $\sim 2$  Myr) and, like Orion, it is located at the surface of a big molecular cloud in a “blister” opened by the radiation of the early stars. These young massive stars and the associated H II region have been known and studied for almost fifty years (Westerlund 1964; Hutchings et al. 1991; Battinelli & Demers 1992; Massey et al. 2000), but very little was known about low-mass objects in the field. Recently, however, thanks to observations made with the *Hubble Space Telescope* (HST) and the *Spitzer Space Telescope*, it has become possible to study the star formation in NGC 602 and surrounding regions over a wide range of masses and this subject has been the topic of a number of recent papers.

Carlson et al. (2007) carried out a panchromatic study of NGC 602 with the HST at optical wavelengths and *Spitzer* in the range  $3.6 - 8.0 \mu\text{m}$  (later extended to  $24 \mu\text{m}$  by Carlson et al. 2011), discovering an extensive population of candidate pre-main sequence (PMS) stars and young stellar objects

(YSOs). Through comparison of the observed magnitudes with theoretical PMS isochrones (although initially not for the metallicity appropriate for the SMC) and with models of the spectral energy distribution of YSOs, they conclude that star formation started about 4 Myr ago in the central cluster and later propagated towards the periphery, where it still continues. A similar conclusion was reached by Gouliermis et al. (2007), whose analysis of archival *Spitzer* mid-infrared observations of an area of  $30 \text{ arcmin}^2$  around NGC 602 reveals 22 YSO candidates, along the rims of the parent molecular cloud. Like Carlson et al. (2007), Gouliermis et al. (2007) attribute the formation of these YSOs to triggering caused by the photoionisation of the young stellar association.

Combining high resolution echelle spectroscopy and velocity maps from a neutral hydrogen (HI) survey (Staveland-Smith et al. 1997) with the HST observations of Carlson et al. (2007), Nigra et al. (2008) tried to establish the likely scenario leading to the formation of NGC 602. These authors do not find morphological evidence of violent events such as supernovae or strong stellar winds. They suggest instead that about 7 Myr ago the interaction of two expanding HI shells created an overdensity, from which NGC 602 started to form about 3 Myr later, and newly formed massive stars started to erode the surrounding nebular material, creating a photodissociation region. These authors speculate that NGC 602 is the result of a single star-forming event, in a region of low gas density. However, as we will show in this work, the star formation history of this region is much more complex than what Nigra et al. (2008) suggested. Indeed, Cignoni et al. (2009) have already shown that, even though the current star formation episode at the centre of NGC 602 (hereafter NGC 602 A) had a peak about 2.5 Myr ago, two neighbouring associations appreciably older than it (NGC 602 B and NGC 602 B2) were formed as part of the same process. According to their analysis, these associations have ages between 15 and 150 Myr (Schmalzl et al. 2008 had previously suggested ages of 80 and 160 Myr for NGC 602 B and NGC 602 B2, respectively).

<sup>1</sup> European Space Agency, Keplerlaan 1, 2200 AG Noordwijk, Netherlands; gdemarchi@rssd.esa.int

<sup>2</sup> European Southern Observatory, Karl-Schwarzschild-Str.2, 85748 Garching, Germany, gbeccari@eso.org

<sup>3</sup> Space Telescope Science Institute, 3700 San Martin Drive, Baltimore, MD 21218, USA, panagia@stsci.edu

<sup>4</sup> INAF-NA, Osservatorio Astronomico di Capodimonte, Salita Moiairiello, 16 80131 Naples, Italy

<sup>5</sup> Supernova Limited, OYV #131, Northsound Rd., Virgin Gorda, British Virgin Islands, VG 1155

<sup>\*</sup> Based on observations with the NASA/ESA *Hubble Space Telescope*, obtained at the Space Telescope Science Institute, which is operated by AURA, Inc., under NASA contract NAS5-26555

To understand how star formation has proceeded in this field, it is crucial to study the properties of PMS stars, particularly of those of lower mass. These objects represent a living record of how star formation has proceeded over the past  $\sim 50$  Myr or more, which is a time span much longer than the one offered by the study of massive stars. All the works cited above have indeed made use of PMS stars to probe recent star formation. However, the selection of PMS objects in those papers is based on a topological analysis in the broadband colour–magnitude diagram (CMD) alone, namely in the  $V$  vs.  $V-I$  plane. Therefore, those studies are limited to the youngest PMS stars, with ages younger than  $\sim 5$  Myr, which are well separated in colour from MS stars. In the CMD, these objects are located to the right of and above the MS. Conversely, any PMS objects older than  $\sim 10$  Myr are very hard to distinguish from the MS itself in the CMD, thereby thwarting any attempt to study other recent star formation episodes in the same field.

On the other hand, thanks to distinctive emission features in the spectra of PMS stars still undergoing mass accretion, we have shown that it is possible to efficiently and reliably identify all objects of this type in a stellar field, regardless of their age and of their position in the CMD. Building on the work of Romaniello (1998), of Panagia et al. (2000), and of Romaniello et al. (2004), De Marchi, Panagia & Romaniello (2010, hereafter Paper I) and De Marchi et al. (2011b, hereafter Paper II) showed that through a suitable combination of broad- and narrow-band photometry an accurate determination of the  $H\alpha$  luminosity of these objects is possible, from which the accretion luminosity and mass accretion rate can be derived. In this work, we apply the methods developed and tested in Papers I and II to investigate how star formation has proceeded in the NGC 602 region.

The structure of the paper is as follows: in Section 2 we describe the observations and the photometric analysis, while we devote Section 3 to the search for PMS stars through their  $H\alpha$  excess emission. In Section 4 we derive the physical parameters for these objects, including effective temperature, luminosity, age, mass and accretion luminosity, while Section 5 addresses the presence of several generations of stars in the field and their mutual relationships. In Section 6 we derive the mass accretion rate and study how it evolves in time. A summary of the most important conclusions of the paper is presented in Section 7.

## 2. OBSERVATIONS AND DATA ANALYSIS

This work is based on observations of a field of  $\sim 3'3 \times 3'3$  around the cluster NGC 602 obtained on 2004 July 14 and 18 with the Wide Field Channel of the Advanced Camera for Surveys (ACS) on board of the HST (proposal nr. 10248, principal investigator A. Nota). The dataset includes observations in the F555W band (hereafter  $V$ ; five exposures for a total duration of 2 153 s), F814W band (hereafter  $I$ ; five exposures for a total of 2 265 s) and N658N band (hereafter  $H\alpha$ ; three exposure for a total of 1 908 s). A suitable dithering pattern and the combination of long and short exposures in the same band provide proper sampling of the point spread function (PSF), while preventing saturation of the brightest stars.

As regards the photometry, we first analysed the  $V$ - and  $I$ -band images, starting from the flat-fielded exposures corrected for geometric distortion and for the effective area of each pixel (see Sirianni et al. 2005 for details). The PSF-fitting procedure DAOPHOT II (Stetson 1987) was applied to each individual frame and a master list of stars was obtained

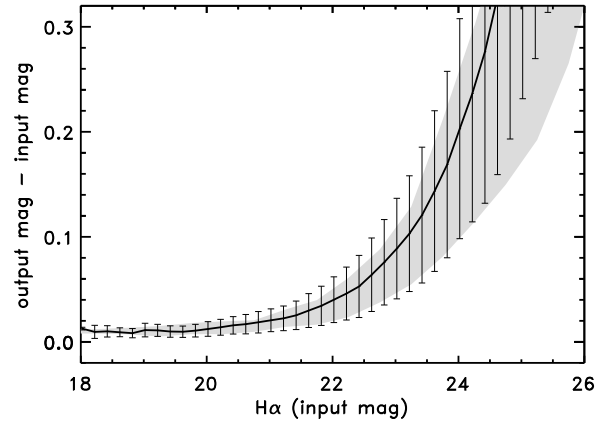


FIG. 1.— Mean of the error distribution of the  $H\alpha$  magnitudes (solid line), and associated  $1\sigma$  uncertainties (error bars), obtained from the comparison between input and output magnitudes in the artificial star experiments. The shaded area shows the distribution of the photometric uncertainties calculated by ALLFRAME.

using all the stars detected in at least six of the ten  $V$ - and  $I$ -band images. We derived in this way an initial catalogue free of spurious detections, such as cosmic rays or haloes and spikes around saturated stars, containing 7 021 objects detected in the  $V$  and  $I$  bands, of which 6 261 are also detected in the  $H\alpha$  band. We furthermore restricted the DAOPHOT II sharpness parameter  $s$  to span the range  $-0.15 \leq s \leq 0.15$ , in order to exclude cosmic rays and extended objects.

The resulting master list, containing 5 788 stars, was then used to perform PSF fitting over the entire dataset, including the  $H\alpha$  images, using the standard ALLFRAME routine (Stetson 1994). The average of the magnitudes measured in each individual frame for every master list object was adopted as the star magnitude in the final catalogue, while we took the resulting standard deviation around the mean for each object as the associated photometric uncertainty (see e.g. Stetson 1987). Down to magnitudes  $V = 21.3$  and  $I = 21.0$  all stars detected in  $V$  and  $I$  are also detected in  $H\alpha$ . This fraction drops to 95 % at  $V = 28.5$  and  $I = 27.3$  and no stars detected in  $H\alpha$  are fainter than these limits.

Since in the case of the  $H\alpha$  images there are only three exposures, we also conducted artificial star tests on those images in order to independently verify the photometric uncertainty (see e.g. Stetson & Harris 1988). We added more than 170 000 artificial stars, spread over several tests and uniformly distributed with a density of one object per 2.3 square arcsec, in order to not alter the crowding conditions of the frames. The input magnitudes of the artificial stars were drawn from a luminosity function similar to the observed one but monotonically extended well beyond the detection limit, in order to increase the statistics for faint stars. We then applied the same photometric procedure used for the original images and compared the input magnitudes with the derived magnitudes, finding an excellent agreement in their values, as shown in Figure 1. The solid line corresponds to the mean difference and the error bars show the  $\pm 1\sigma$  uncertainties. In the analysis that follows we will take these as photometric uncertainties in the  $H\alpha$  band. In the  $V$  and  $I$  bands the photometric uncertainties are considerably smaller, owing to the wider pass bands. We also show for reference in Figure 1 the photometric uncertainty (shaded area) as derived by ALLFRAME, which is slightly smaller than those derived through artificial star experiments, as expected (see e.g. Beccari et al. 2013). In

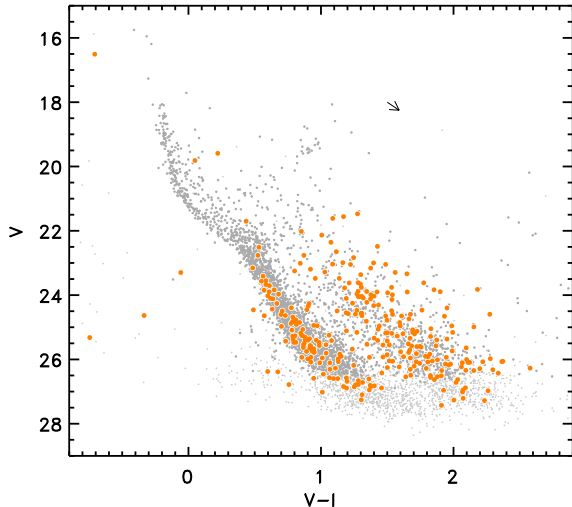


FIG. 2.— CMD of all stars after correction for reddening. All stars, except for those indicated by the smallest grey dots, have a combined photometric uncertainty in  $V$  and  $I$  of 0.1 mag or less. Objects indicated as thick dark dots (orange in the online version) correspond to stars with  $H\alpha$  excess emission (see Section 3).

summary, the artificial star experiments gave us general confidence that the uncertainties assigned by our photometry to the magnitudes of individual stars is realistic, also in the  $H\alpha$  band.

The final catalogue contains a total of 5 500 stars, with well defined magnitudes in the  $V$ ,  $I$  and  $H\alpha$  bands, which were calibrated into the VEGAMAG photometric system according to the procedures described in Sirianni et al. (2005) and using the most current photometric zero points (Bohlin 2012).

The outcome of our photometry is the CMD of the entire field, as shown in Figure 2. Having defined the combined photometric uncertainty in the  $V$  and  $I$  bands as:

$$\delta_2 = \sqrt{\frac{\delta_V^2 + \delta_I^2}{2}}, \quad (1)$$

objects with  $\delta_2 < 0.1$  mag are indicated as larger grey dots, whereas smaller grey dots are used for the remaining stars (objects marked as thick dark dots, orange in the online version, correspond to stars with  $H\alpha$  excess emission and are discussed in Section 3). The magnitudes shown in the CMD (and in all figures thereafter) have already been corrected for the effects of interstellar extinction. Adopting the canonical value of  $E(B-V) = 0.08$  (see Carlson et al. 2007 and Schmalzl et al. 2008, and references therein, for an extensive discussion of the extinction in this region), and assuming that the reddening law derived by Scuderi et al. (1996) for the field of SN 1987A also applies to this region of the SMC, we obtain  $A_V = 0.25$ ,  $A_I = 0.16$  and  $A_{H\alpha} = 0.21$  for the specific ACS bands used here. The corresponding reddening vector is shown by the small arrow in Figure 2.

### 3. SEARCHING FOR PRE-MAIN SEQUENCE STARS

The CMD of Figure 2 reveals that in the field covered by these observations there are stars of different ages: there are young massive stars in the upper MS (with  $V-I < 0$  and  $V \lesssim 21$ ), there are objects brighter and redder than the MS, in the region usually occupied by PMS stars, and there are stars in the lower MS and along what appears as the red-giants

branch with a prominent red clump at  $V \simeq 19$ , which are usually populated by older objects. This variety of stellar populations has already been considered and discussed in a number of recent papers (see Carlson et al. 2007; Schmalzl et al. 2008; Cignoni et al. 2009; Gouliermis et al. 2012). Note that, owing to the high Galactic latitude of the SMC, the contamination due to foreground Milky Way sources is insignificant. According to the Besançon Galactic stellar population synthesis models (Robin et al. 2003), only four foreground stars with magnitudes in the range  $7 < M_V < 20$  should be present towards NGC 602 in a field of the size covered by our observations.

As mentioned in the Introduction, all these works identify as PMS stars all objects located appreciably to the right of the MS and above it. In this paper, however, for the first time we look for the signs of the active mass accretion process that is expected to accompany the PMS phase and that is responsible for the strong excess emission normally observed in objects of this type (e.g. Calvet et al. 2000). In particular, following the method developed in Papers I and II, we have looked for the presence of an excess in the  $H\alpha$  emission line by using a combination of broad-band ( $V, I$ ) and narrow-band ( $H\alpha$ ) photometry. This way of identifying PMS stars is more reliable than the simple classification based on the position of the objects in the CMD or Hertzsprung–Russell (H–R) diagram and provides for a secure detection of relatively old PMS stars, already close to the MS.

As explained in Paper I, the majority of stars in a typical stellar field have no excess  $H\alpha$  emission. Therefore, the median value of the  $V-H\alpha$  colour index at a given effective temperature  $T_{\text{eff}}$  defines a spectral reference template for all stars with that  $T_{\text{eff}}$  and can be used to identify objects with  $H\alpha$  excess. In practice, the  $V-H\alpha$  vs.  $V-I$  diagram shown in Figure 3 can be used for this purpose. Stars shown as light grey dots are objects with a combined photometric uncertainty  $\delta_3 \leq 0.08$  mag, where

$$\delta_3 = \sqrt{\frac{\delta_V^2 + \delta_{H\alpha}^2 + \delta_I^2}{3}} \quad (2)$$

and  $\delta_V$ ,  $\delta_{H\alpha}$  and  $\delta_I$  are the photometric uncertainties in the corresponding bands. A total of 1906 objects satisfy this condition, with the most stringent constraint being set by the uncertainty in  $H\alpha$  (the typical uncertainty in the other two bands are less than 0.02 mag). The log-dashed line represents the median  $V-H\alpha$  colour obtained as the running median with a box-car size of 100 points (the box-car size is reduced to 10 points for  $V-I > 1.5$ , where there are fewer stars). It is reassuring to see that the reference template empirically defined by the dashed line is in remarkably good agreement with the model atmospheres of Bessell et al. (1998), shown by the thick solid line for this specific ACS filter set.

In order to find stars with  $H\alpha$  excess emission, it is sufficient to look for objects with a  $V-H\alpha$  index exceeding that of the reference template at the same  $V-I$  in a significant way. As in previous works (e.g. Papers I and II; Beccari et al. 2010; De Marchi et al. 2011c; Spezzi et al. 2012, hereafter Paper III), we set this limit at the  $4\sigma$  level and looked for stars that exceed the reference template by at least four times their  $V-H\alpha$  photometric uncertainty. Indicating with  $(V-H\alpha)^{\text{obs}}$  the observed value and with  $(V-H\alpha)^{\text{ref}}$  the value on the reference template at the same  $V-I$  colour, we define their difference as

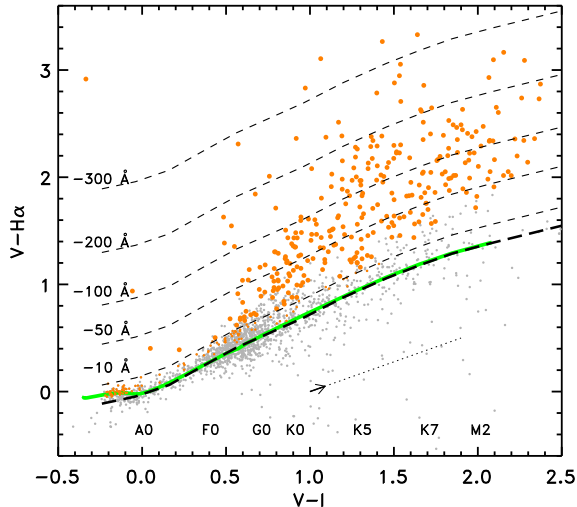


FIG. 3.— Two-colour diagram of the stars with  $\delta_3 \leq 0.08$  mag (light grey dots), corrected for reddening. The thick long-dashed line represents the running median  $V-H\alpha$  colour, whereas the thick solid line (green in the online version) shows the model atmospheres of Bessell et al. (1998). All objects indicated as large dark dots (orange in the online version) have a  $V-H\alpha$  excess larger than  $4\sigma$  and an  $H\alpha$  excess equivalent width of more than  $10\text{ \AA}$ . The 10, 50, 100, 200, and  $400\text{ \AA}$  limits are shown by the short-dashed lines and labelled accordingly. Objects indicated as small dark dots (orange in the online version) also have a  $V-H\alpha$  excess larger than  $4\sigma$  but less than  $10\text{ \AA}$  for the  $H\alpha$  equivalent width. The short arrow shows reddening vector for  $A_V = 0.25$ , whereas the dotted line extends it by a factor of ten purely to show that its direction is almost parallel to that of the reference template. Spectral types for objects in the range  $0 < V-I < 2$  are also indicated.

$$\Delta H\alpha = (V-H\alpha)^{\text{obs}} - (V-H\alpha)^{\text{ref}} \quad (3)$$

Then the condition to be satisfied for considering the star a bona-fide PMS object is that  $\Delta H\alpha > 4\sigma_{VH\alpha}$ , where  $\sigma_{VH\alpha}$  is the photometric uncertainty on the  $(V-H\alpha)^{\text{obs}}$  colour. A total of 400 objects satisfy this condition and they are shown in Figure 3 as large dots (orange in the online version).

As mentioned above, all magnitudes in Figure 3 are corrected for extinction using the average value  $A_V = 0.25$  for all stars and the reddening law of Scuderi et al. (1996). The reddening vector for  $A_V = 0.25$  is shown by the small arrow, like in Figure 2, but for better illustrating its direction we have extended it with the dotted line by a factor of ten, in order to show that the vector is almost parallel to the reference template. This means that even relatively large fluctuations in the reddening correction of individual stars, due for instance to patchy absorption, would not significantly affect the identification of stars with  $H\alpha$  excess.

All these stars have a robust  $H\alpha$  excess emission and as such they are candidate PMS objects. However, to further restrict the list to the most certain PMS stars, following White & Basri (2003), Paper I and Barentsen et al. (2011), we conservatively limit our selection to stars which also have an equivalent width of the  $H\alpha$  emission line of more than  $10\text{ \AA}$ , or  $W_{\text{eq}}(H\alpha) < -10\text{ \AA}$  if, as customary, negative values of the equivalent width are used for emission lines. According to White & Basri (2003),  $W_{\text{eq}}(H\alpha) < -10\text{ \AA}$  is a clear sign of accretion in genuine T Tauri stars of spectral type earlier than M2.5 (roughly  $V-I = 2.3$  for the specific ACS filters), since it cannot be caused by chromospheric activity.

As regards the equivalent widths, we derive them directly

from the colour difference between the  $V-H\alpha$  index of the star and that of the reference template in Figure 3 and from the properties of the  $H\alpha$  filter, as explained in detail in Paper I. More precisely, if the stars defining the reference template had no  $H\alpha$  absorption features, their  $V-H\alpha$  colour would correspond to that of the pure continuum and could be directly used to derive the equivalent width of the  $H\alpha$  emission line,  $W(H\alpha)$ . As explained in Paper I, although certainly valid for stars with large  $H\alpha$  excess, this assumption is not true in general. Instead, given the excellent agreement between the reference template and the model atmospheres of Bessell et al. (1998), we can use the a modified version of the latter, with the  $H\alpha$  emission line suppressed, to derive the magnitude of the sole continuum in the specific  $H\alpha$  band of the ACS, as a function of spectral type or  $V-I$  colour. Since the  $H\alpha$  line profile is very narrow when compared to the width of the filter, the equivalent width is simply given by the relationship:

$$W_{\text{eq}}(H\alpha) = RW \times [1 - 10^{-0.4 \times (H\alpha - H\alpha^c)}] \quad (4)$$

where  $RW$  is the rectangular width of the filter (similar in definition to the equivalent width of a line), which depends on the characteristics of the filter,  $H\alpha$  is the measured magnitude and  $H\alpha^c$  the magnitude of the sole continuum. The value of  $RW$  for the ACS F658N filter used here is  $74.98\text{ \AA}$  and values for the  $H\alpha$  bands of current and past HST instruments are given in Paper I.

A small correction is then applied to the derived  $W_{\text{eq}}(H\alpha)$  values to account for the fact that for normal stars (those in grey in Figure 3) the  $H\alpha$  line is normally in absorption (see Paper I). The stars with  $W_{\text{eq}}(H\alpha) < -10\text{ \AA}$  are shown as large orange dots in Figure 3, and are located above the short dashed line corresponding to  $W_{\text{eq}}(H\alpha) = -10\text{ \AA}$ . In total we find 296 objects redder than  $V-I = 0$  that satisfy this condition, with a median equivalent width  $W_{\text{eq}}(H\alpha) \simeq -60\text{ \AA}$  and a median  $H\alpha$  luminosity  $L(H\alpha) \simeq 2.4 \times 10^{-3} L_{\odot}$ . Hereafter, we take these objects as bona-fide PMS stars. The median  $W_{\text{eq}}(H\alpha)$  and  $L(H\alpha)$  values might appear larger than those typical of Galactic T-Tauri stars, but as explained above our sample only includes objects with  $W_{\text{eq}}(H\alpha) < 10\text{ \AA}$  and therefore stars with low  $L(H\alpha)$  are automatically excluded.

These objects are shown in the CMD of Figure 2 as large dots (orange in the online version). Interestingly, not all of them are in the region occupied by young PMS stars, i.e. brighter and redder than the MS, as some are very close to or at the MS itself. This is a consistent feature of all the star-forming regions previously observed by us in the Magellanic Clouds and in the Milky Way (e.g. Panagia et al. 2000; Papers I and II; Beccari et al. 2010; De Marchi et al. 2011c; Paper III). Several types of  $H\alpha$  emitting sources could occupy the MS region the CMD but, as we will now show, the most likely explanation is that these are older PMS stars, approaching the MS and still actively accreting.

Examples of objects with  $H\alpha$  excess in this region of the CMD include cataclysmic variables (CVs) and stars with active chromospheres, such as RS CVn objects or dMe stars. Chromospheric activity, however, can be immediately ruled out, because it causes very weak  $H\alpha$  emission for stars earlier than spectral type M2, with equivalent widths typically of order  $-1\text{ \AA}$  (e.g. Bopp & Talcott 1978; Bopp & Schmitz 1978). Precisely, it is to keep our sample free from objects of this type that, following White & Basri (2003), we only consider stars with  $W_{\text{eq}}(H\alpha) < -10\text{ \AA}$ .

On the other hand, CVs have typical  $W_{\text{eq}}(H\alpha)$  in the same range as the one we measure (e.g. Warner 1995 and references therein), but these objects are very infrequent. Pretorius & Knigge (2008) searched for objects with  $H\alpha$  excess in the  $R-H\alpha$  vs.  $R-I$  diagram (similar to our Figure 3), using observations from the AAO/UKST SuperCOSMOS  $H\alpha$  Survey (Parker et al. 2005). They analysed the  $R$  and  $H\alpha$  photometry down to  $R = 17$  in 175 regions, each 4 deg on a side, for a total covered area of  $\sim 2800 \text{ deg}^2$  at low Galactic latitudes ( $|b| < 2 \text{ deg}$ ). Each region contains of order 170 000 stars, for a total of about 30 million objects, and only 14 CVs were found amongst them, with an implied frequency of order  $5 \times 10^{-7}$ . Considering that the typical distance to these CVs is  $\sim 500 \text{ pc}$  (Pretorius & Knigge 2008), the  $R = 17$  magnitude limit for these stars translates to about  $R = 27.5$  at the distance of NGC 602 and as such it is very similar to the detection limit of our photometry. Therefore, with a total of 5 500 stars in our field we should expect essentially no (0.003) CVs.

Considering that the metallicity of the stars in the SMC is about a factor of five lower than that of the objects in the Galactic plane, we have also looked at the fraction of CVs in Galactic globular clusters (GC), which have lower metallicity. The cluster 47 Tuc, with  $[Fe/H] = -0.76$  (Harris 1996), offers conditions very similar to those of the SMC field. This cluster contains the largest known number of CVs in a GC (Downes et al. 2005), most of which are located near the cluster centre (Heinke et al. 2005). Inside a field of  $3'4 \times 3'4$  around the cluster centre, observed with the HST as part of the ACS Globular Clusters Survey (Sarajedini et al. 2007), there are in total  $\sim 100\,000$  stars down to  $V \simeq 24$ . Of these stars, 30 are classified as CVs from their X-ray properties (Heinke et al. 2005) and only six of them have excess emission in  $H\alpha$  with  $W_{\text{eq}}(H\alpha) < -20 \text{ \AA}$  (Beccari et al. 2013), with an implied frequency of  $6 \times 10^{-5}$ . Therefore, with a total of 5 500 stars, the expected number of CVs in our field (0.3) remains insignificant.

In summary, it is possible (and perhaps even likely) that some of the stars with  $H\alpha$  excess bluer than the MS in Figure 2 are objects of this type. Precisely for that reason we do not consider any objects with  $H\alpha$  excess bluer than  $V-I = 0$  in this work. However, it is clear that CVs cannot be responsible for the large population of objects with  $H\alpha$  excess near the MS. As concluded in the previous works in this series, the most likely nature of these objects is that they are recently formed stars still actively accreting while they approach the MS. In the next section we will derive the physical properties of these and of the younger PMS stars through comparison with PMS evolutionary models.

#### 4. PHYSICAL PARAMETERS OF THE PMS STARS

The luminosities ( $L$ ) and effective temperatures ( $T_{\text{eff}}$ ) of all stars with photometric uncertainty in  $V$  and  $I$  smaller than 0.1 mag are shown in the H-R diagram (Figure 4) as light grey dots, whereas PMS stars are shown as dark dots (orange in the online version; note that the size of the dots is proportional to the mass accretion rate, as explained later). Effective temperatures are determined by fitting the dereddened  $V-I$  colours of the stars with the ones computed for the same HST bands using stellar atmosphere models. We have adopted the model atmospheres of Bessell et al. (1998) for the metallicity  $[M/H] = -0.5$  appropriate for the SMC, as they provide a well-tested, homogeneous set covering the temperature interval between 3 500 and 50 000 K in the wavelength range

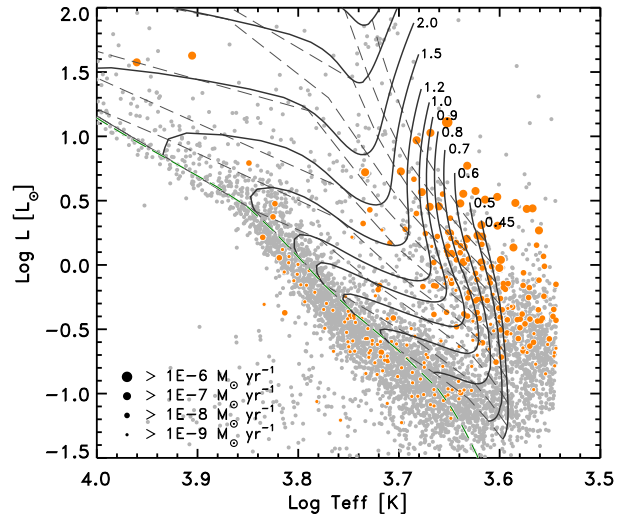


FIG. 4.— All objects with combined photometric uncertainty smaller than 0.1 mag in  $V$  and  $I$  are shown in grey in the H-R diagram. Bona-fide PMS stars are shown as dark dots (orange in the online version), with a symbol size proportional to their mass accretion rate, as per the legend. Thick solid lines show the evolutionary tracks for metallicity  $Z = 0.004$  and masses as indicated. The corresponding isochrones are shown as thin dashed lines, for ages of 0.125, 0.25, 0.5, 1, 2, 4, 8, 16, 32, and 64 Myr from right to left. The constant logarithmic age step has been selected in such a way that the typical distance between isochrones is larger than the photometric uncertainties. The leftmost dashed line (green in the online version) is the ZAMS from the models of Marigo et al. (2008) for the assumed  $Z = 0.004$  metallicity.

between  $90 \text{ \AA}$  and  $160 \mu\text{m}$ . The dereddened magnitudes are then compared with the absolute magnitudes of the models of Bessell et al. (1998) computed for the same bands. These models were renormalised by Romaniello et al. (2002; see their Table 6) in order to provide the absolute magnitudes of stars of a given temperature and surface gravity, for a radius of  $1 R_{\odot}$  and a distance of 10 pc. Knowing the distance to each source, we can derive its radius  $R_*$  since the magnitude difference  $\Delta M_V$  scales as  $\Delta M_V = 5 \times \log(R_*/R_{\odot})$ . Finally, the bolometric luminosity is derived knowing the distance to the objects, from the stellar radius and effective temperature, compared to those of the sun (see Romaniello et al. 2002 for further details). As for the distance to the SMC, we have assumed a distance modulus of  $18.92 \pm 0.03$  corresponding to  $\sim 61 \text{ kpc}$  (Hilditch et al. 2005; Keller & Wood 2006). Note that the sharp cut-off at  $\log T_{\text{eff}} = 3.55$  in Figure 4 is caused by the limited extent of the model atmospheres and, therefore, all objects redder than  $V-I \simeq 2.1$  are ignored.

We also show in Figure 4 the evolutionary tracks (thick solid lines) and isochrones (dashed lines) from the PMS evolutionary models of the Pisa group (Degl’Innocenti et al. 2008; Tognelli et al. 2012). The models have been calculated for  $Z = 0.004$ ,  $Y = 0.24$  and the mixing-length parameter  $\alpha = 1.9$  for masses in the range  $0.45 - 5.5 M_{\odot}$ . As shown by Cignoni et al. (2009), with the assumed distance modulus and reddening  $E(B-V) \simeq 0.08$  and this choice of the metallicity, the Padua isochrones (Fagotto et al. 1994; Marigo et al. 2008) provide an excellent fit to the upper MS. This metallicity also nicely agrees with the currently accepted values for the SMC, which range from  $\sim 1/5$  to  $\sim 1/8 Z_{\odot}$  (see Russell & Dopita 1992; Rolleston et al. 1999; Lee et al. 2005; Perez-Montero & Diaz 2005).

It should be noted, however, that this metallicity is a factor of two higher than that implied by the observations of

NGC 346, in the bar of the SMC, where a metallicity value of  $Z = 0.002$  is preferable (see Paper II). This difference is also consistent with the available measurements of the ratio between extinction and column density of neutral hydrogen  $A_V/N(HI)$ . From Gordon et al. (2003), expressing  $N(HI)$  in units of  $10^{22} \text{ cm}^{-2}$ , we find the ratio to be  $1.35 \pm 0.22$  in the SMC wing and a value about a factor of two lower in the SMC bar ( $0.76 \pm 0.06$ ). Assuming that the ratio scales linearly with metallicity (e.g. Scuderi et al. 1996), this result suggests indeed a factor of  $\sim 2$  higher metal content in NGC 602 than in NGC 346.

In Figure 4, the masses corresponding to the individual tracks are indicated on the right-hand side, whereas the ages of the isochrones increase by a factor of two at each step, starting from 0.125 Myr at the right end to 64 Myr at the left end. We also show for comparison the zero age MS of Marigo et al. (2008) for the same metallicity (leftmost dashed line, in green in the online version).

The comparison with the Pisa models immediately suggests ages older than  $\sim 32$  Myr for most of the PMS stars close to the MS, ages younger than  $\sim 4$  Myr for the rest and few objects in between. Concerning the masses, the majority of PMS stars appear to be less massive than  $\sim 0.8 M_\odot$ . Using a finer grid of models than the one shown in Figure 4, we derived a more accurate measure of the mass and age for 276 PMS stars, excluding the 20 coolest objects that would have required a rather uncertain extrapolation beyond the limits of the theoretical models (see Romaniello 1998 for details on the method used, with an approach similar to the one recently presented by Da Rio et al. 2012). While an accurate determination of the absolute age and mass of individual objects will require spectroscopy only possible with future instrumentation (e.g. the James Webb Space Telescope; Gardner et al. 2006), we can nonetheless derive important information on the properties of star formation in this field by comparing relative ages and masses of groups of stars. Histograms with the age and mass distribution for the 276 stars are shown in Figures 5a and 5b, respectively. Besides the remarkable paucity of stars in the  $\sim 10$ – $30$  Myr range, already seen in the H–R diagram, Figure 5a shows that about 1/3 of our PMS objects have isochronal ages older than  $\sim 30$  Myr. The double peak seen in the figure implies that in the past this region underwent at least one and possibly several bursts of star formation, likely as intense as the one currently revealed by the 0–2 Myr old objects. We will come back to this point in Section 5.

The  $\Delta H\alpha$  parameter defined in the previous section also allows us to easily derive the  $H\alpha$  emission line luminosity  $L(H\alpha)$  for these stars. As explained in Paper I,  $L(H\alpha)$  is obtained from  $\Delta H\alpha$ , from the photometric zero point and absolute sensitivity of the instrumental set-up and from the distance to the sources. As for the latter, we have assumed a distance modulus  $(m-M)_0 = 18.92$  as mentioned before, whereas the photometric properties of the instrument are as listed in the ACS Instrument Handbook (Maybhatte et al. 2010). The median  $L(H\alpha)$  in our sample is  $\sim 2 \times 10^{-3} L_\odot$ , with the 17 and 83 percentile levels in the distribution at  $0.001 L_\odot$  and  $0.01 L_\odot$ , respectively. We stress here that, although our sample only includes objects with  $W_{\text{eq}}(H\alpha) < -10 \text{ \AA}$ , the  $L(H\alpha)$  values that we find are in excellent agreement with those of Galactic stars of similar mass. Dahm (2008) analysed the  $H\alpha$  luminosity of a group of T Tauri stars in Taurus–Auriga, taken from the original sample of Valenti et al. (1993), with masses similar to those of the objects in our sample. He

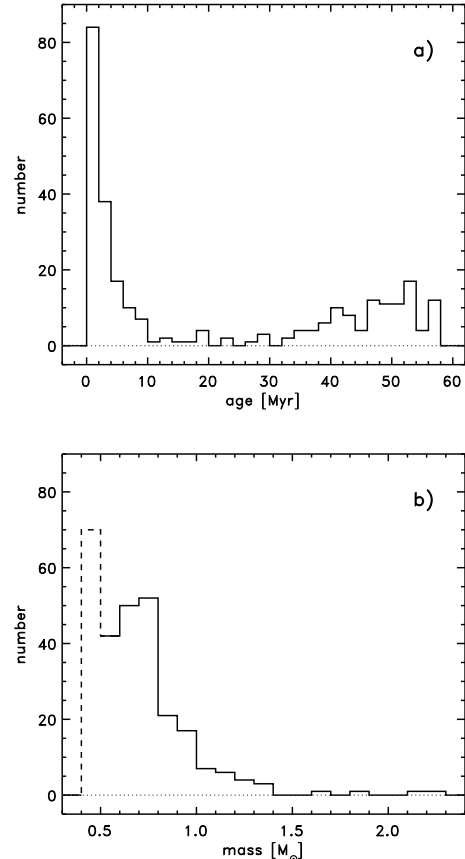


FIG. 5.— Age and mass distribution of PMS stars. The first mass bin is shown with a dashed line because it could also include stars of lower mass.

obtains  $L(H\alpha)$  luminosities ranging from  $0.001 L_\odot$  (17 percentile) to  $0.014 L_\odot$  (83 percentile), in excellent agreement with our measurements.

The uncertainty on  $L(H\alpha)$  is typically  $\sim 12\%$  and is completely dominated by the statistical uncertainty on the  $H\alpha$  photometry (10%), with the distance accounting for 5% (Hilditch et al. 2005; Keller & Wood 2006) and the absolute sensitivity of the instrumental setup for another 3%. These values are corrected for the small contribution from the [NII] emission features at  $6548 \text{ \AA}$  and  $6584 \text{ \AA}$  that are included in the rather wide F658N passband of the ACS. The correction is very small, only 2.1%, but since it is a systematic effect it is a good practice to apply it.

Having measured  $L(H\alpha)$  we can derive another important physical parameter for the PMS stars, namely the accretion luminosity  $L_{\text{acc}}$ . As discussed in Paper I, Dahm’s (2008) logarithmic best fit to the  $\log L_{\text{acc}}$  vs.  $\log L(H\alpha)$  plane would provide a slope of  $1.18 \pm 0.26$  for such a relationship. On the other hand, theoretical models (e.g. Muzerolle et al. 1998) would predict logarithmic slopes of about unity for low accretion rates, i.e. faint  $L(H\alpha)$ , and shallower slopes for higher luminosities. In the absence of compelling evidence in favour or against a steep slope, we adopt a logarithmic slope of unity for the empirical  $\log L_{\text{acc}}$  vs.  $\log L(H\alpha)$  relationship, which is inside the uncertainty band on Dahm’s (2008) value. In their recent study of accretion rates for T Tauri stars using nearly simultaneous ultraviolet and optical observations, Ingleby et al. (2013) find consistently a slope of unity. Not only for the luminosity in  $H\alpha$  ( $1.0 \pm 0.2$ ), but also for other important ac-

cretion indicators, namely the luminosity in  $H\beta$  ( $1.0 \pm 0.1$ ), Ca II K ( $1.0 \pm 0.2$ ), C II] ( $1.1 \pm 0.2$ ) and Mg II ( $1.1 \pm 0.2$ ). A choice of unity has a physical meaning and implies that a constant fraction of the gravitational energy released in the accretion process goes into  $H\alpha$  emission. In Paper I and II we determined the proportionality constant from the data summarised by Dahm (2008), combined with the dispersion measured for the stars in NGC 346, finding

$$\log L_{\text{acc}} = (1.72 \pm 0.25) + \log L(H\alpha). \quad (5)$$

We will make use of  $L_{\text{acc}}$  obtained in this way in Section 6 for deriving the mass accretion rate  $\dot{M}_{\text{acc}}$ . The median value of  $L_{\text{acc}}$  that we find for the PMS stars in our sample is  $\sim 0.1 L_{\odot}$ . Comparing this value to the typical bolometric luminosities  $L_{\text{bol}}$  of these objects, we find the median  $L_{\text{acc}}/L_{\text{bol}}$  ratio to be  $\sim 0.3$ . The 17 and 83 percentiles, which in a Gaussian distribution would correspond to the  $\pm 1\sigma$  values, are respectively 0.15 and 0.63. The derived  $L_{\text{acc}}/L_{\text{bol}}$  ratio indicates that in our sample the accretion luminosity does not dominate the total stellar luminosity, as is expected of stars that are no longer in the embedded phase (e.g. Nisini et al. 2005; Antonucci et al. 2008). Taking again Valenti et al.'s (1993) sample of PMS stars in Taurus–Auriga, the median  $L_{\text{acc}}/L_{\text{bol}}$  ratio is  $\sim 0.15$ , whereas the corresponding value in our sample is  $\sim 0.3$  or a factor of two higher. However, as explained above, we restrict our analysis to stars with  $W_{\text{eq}}(H\alpha) < -10 \text{ \AA}$ , thereby excluding all objects with small  $H\alpha$  excess and small  $H\alpha$  luminosity, and therefore it is to be expected that we will miss objects with small accretion luminosity.

## 5. STAR FORMATION ACROSS TIME AND SPACE

As discussed in Section 3, the age distribution of the PMS stars in our sample is bimodal (see Figure 5a). About 1/2 of the objects appear younger than  $\sim 5 \text{ Myr}$  and about 1/3 older than  $\sim 30 \text{ Myr}$ , with few objects (50) at intermediate ages. These ages are based on the comparison of the observations with theoretical isochrones and, as such, they are subject to uncertainties. Besides photometric errors and uncertainties in the input physics affecting the models, there are other physical effects that could cause an incorrect determination of the age (or mass) of individual objects. These include for instance unresolved binaries, differential reddening, stellar variability, veiling resulting from accretion, and scattering due to a disc seen at high inclination. All these effects combine to produce a broadening in the H–R diagram, which could be misinterpreted as an age spread (see e.g. Hennekemper et al. 2007 and Da Rio et al. 2010).

In fact, even though all the effects mentioned above could mimic an age spread, none of them can produce the clearly bimodal distribution that we observe in the H–R diagram. The remarkable paucity of PMS stars with age comprised between the 4 Myr and 16 Myr isochrones (already evident in Figure 4) is quantified in Figure 6, where we show the distribution of PMS stars as a function of the difference in their  $\log T_{\text{eff}}$  values. The distribution is obtained by counting the number of PMS stars in strips parallel to the zero-age MS (ZAMS), starting from the dot-dashed line, and it is clearly bimodal, with two peaks separated by several times their width. A Gaussian fit to the two peaks (dot-dashed lines in Figure 6b) gives  $\sigma_1 = 0.020 \text{ dex}$  for older PMS stars and  $\sigma_2 = 0.025 \text{ dex}$  for younger PMS stars. The separation between the two peaks (0.1 dex) corresponds to respectively 5 and 4 times these

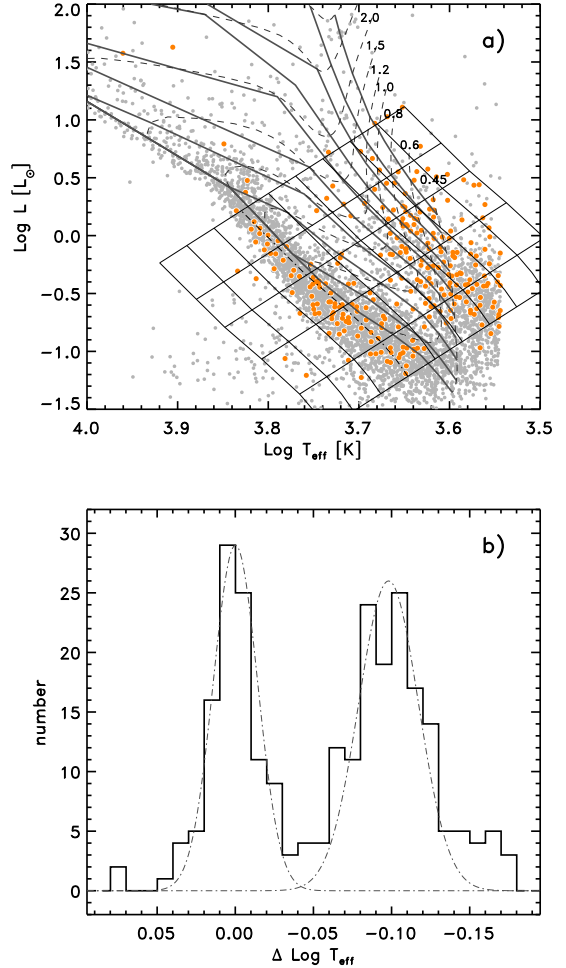


FIG. 6.— Distribution of PMS stars in the H–R diagram obtained by counting the number of objects falling in strips parallel to the ZAMS. The grid shown in panel a) corresponds to  $\Delta \log T_{\text{eff}} = 0.03$ , for display purposes, but the histograms in panel b) are obtained using a finer grid ( $\Delta \log T_{\text{eff}} = 0.01$ ). The value of  $\Delta \log T_{\text{eff}} = 0$  corresponds to the dot-dashed line in panel a). The thin dot-dashed lines in panel b) show a Gaussian fit to the two peaks.

widths and confirms that the two distributions are clearly distinct.

Physically, it is hard to imagine a mechanism that would affect the temperatures and luminosities of stars in such a way that they are selectively displaced from the region occupied by young PMS objects in the H–R diagram and moved towards the MS, while leaving only a handful of them in the region in between. Therefore, while the effects mentioned above can introduce uncertainties on the relative ages of individual objects (in Paper I these are estimated to be typically no more than a factor of  $\sqrt{2}$ ), we can safely conclude that the two groups of stars with  $H\alpha$  excess seen in the H–R diagram must belong to different generations, with ages that differ by much more than a factor of two and likely up to an order of magnitude.

### 5.1. Multiple stellar generations

A histogram of the age distribution was already shown in Figure 5a. Considering the uncertainties inherent in our age determination, stemming from the comparison of model isochrones with our photometric data, the histogram in Figure 7 offers a more realistic representation of the relative age

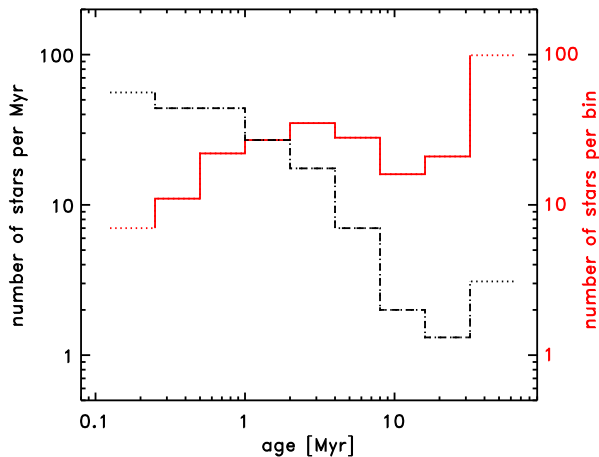


FIG. 7.— Histograms showing the number of stars per age bin (thick solid line, red in the online version) and the apparent star formation rate, i.e. the number of stars per Myr (dot-dashed line), as a function of age. Only bona-fide PMS stars with  $H\alpha$  excess emission in the range  $0.4\text{--}2.5 M_{\odot}$  are considered.

distribution, with ages binned using a constant logarithmic step (a factor of 2). The solid line gives the actual number of stars contained within each age bin, while the dot-dashed line provides a measurement of the apparent star formation rate, obtained by dividing the number of objects in each bin by the width of the bin itself (we use a dotted line at the extremes of the distribution to indicate larger uncertainties).

Note that the dot-dashed line in Figure 7 clearly provides a lower limit to the star formation rate. First of all, crowding effects, particularly in the proximity of massive stars, make the detection of faint low-mass PMS stars more difficult. Furthermore, here we only consider PMS stars in the range  $0.4\text{--}2.5 M_{\odot}$  having  $H\alpha$  excess emission at the  $4\sigma$  level or more at the time of the observations. Since the strength and equivalent width of the  $H\alpha$  emission line are highly variable in time (e.g. Fernandez et al. 1995; Smith et al. 1999; Alencar et al. 2001), the objects that at any given time show  $H\alpha$  excess emission at these levels are necessarily only a fraction of the total population of PMS stars.

Assuming that all objects cooler than the 5 Myr isochrone in the  $H\text{--}R$  diagram of Figure 6a are PMS stars, we find that the fraction of those with  $H\alpha$  excess emission is  $\sim 15\%$ . Therefore, for young stars, the upper limit to the number of PMS objects is  $\sim 6.5$  times larger than what we measure. As regards older PMS stars, one expects the fraction of objects with  $H\alpha$  excess to be lower than for younger stars. Indeed, as we will show in Section 5.3, for two older clusters in the field this fraction is  $\sim 8\%$  along the MS in the range  $24 < V < 27$ . Thus, the actual number of PMS stars for ages older than  $\sim 20$  Myr is at most  $\sim 12.5$  times larger than what we measure, since the stars without excess along the MS may include much older field stars.

Near the peak of the distribution in Figure 7, at  $\sim 0.5$  Myr, the lower limit to the star formation rate is  $\sim 3 \times 10^{-5} M_{\odot} \text{ yr}^{-1}$  (the median mass of those objects is  $\sim 0.6 M_{\odot}$ ). The corresponding upper limit is  $\sim 6.5$  times this value, i.e.  $\sim 2 \times 10^{-5} M_{\odot} \text{ yr}^{-1}$ , in excellent agreement with that found by Cignoni et al. (2009) for this cluster. At  $\sim 20$  Myr the lower limit to the rate drops by a factor of 30 to  $\sim 10^{-6} M_{\odot} \text{ yr}^{-1}$  (me-

dian mass  $\sim 1 M_{\odot}$ ), although the corresponding upper limit is about an order of magnitude higher.

In spite of the uncertainties on the age of the individual objects mentioned above, it is clear that beyond  $\sim 30$  Myr a highly significant increase is seen, both in the star formation rate ( $\times 2.5$ ) and in the number of stars per bin ( $\times 5$ ). This indicates that the current burst is not the only one in this area and it might not even be the most prominent one, since the total integrated output of stars older than  $\sim 30$  Myr and those younger than a few Myr (solid line) is comparable. In fact, if the fraction of PMS stars with  $H\alpha$  excess has an exponential decay with time (Fedele et al. 2010), episodes occurring more than 30 Myr ago might have contributed a large portion of the stars in this region. Since the accuracy on relative ages is of order a factor of  $\sqrt{2}$  (Paper I), it is not possible to estimate exactly how long the previous burst lasted nor how many short bursts took place in the time frame of  $\sim 30$  Myr covered by the last age bin. Therefore, if there was just one burst, the star formation strength might have been considerably higher than that of the current episode.

Besides very different ages, the two populations of younger and older PMS stars also have considerably different spatial density distributions. We compare these distributions to one another in Figure 8 by means of contour lines of stellar density with logarithmic steps, overlaid on a true-colour image of the region. Out of the total population of 276 PMS stars with well defined masses and ages, we have selected all those younger than 5 Myr (a total of 132 objects, cyan in the online version) and those older than 20 Myr (in total 111 objects, orange in the online version). The contour plots shown for each of these groups in Figure 8 were obtained after smoothing the actual distribution with a Gaussian beam with size  $\sigma = 4''$  or  $\sim 1.2$  pc, as indicated by the circle at the bottom of the figure. The lowest contour level corresponds to a local density of PMS stars three times as high as the average PMS stars density over the entire field. The steps between contour levels are constant and corresponds to a factor of 2. We also show with small dots (yellow in the online version) the positions of 34 stars with ages between 5 and 20 Myr.

The remarkable feature in this figure is the difference in the spatial distribution of younger and older PMS stars: older objects are much more widely distributed and, except for the centre of NGC 602, they do not always overlap with the younger generation. This difference confirms that episodic accretion (e.g. Baraffe et al. 2009, 2010) is not at the origin of the bimodal distribution of PMS stars in Figure 6, since it would otherwise require a rather contrived spatial separation of stars with different accretion histories. In the following sections we discuss the two groups of objects in more detail.

## 5.2. Younger PMS stars

PMS stars younger than  $\sim 5$  Myr, traced by the cyan contours in Figure 8, are preferentially located near the central cluster NGC 602 A, which also contains the bulk of massive stars. Furthermore, the younger PMS stars are distributed in a number of small groups, some of which match the concentrations of unresolved YSOs recently identified by Carlson et al. (2011) in their panchromatic study of these regions covering wavelengths from 0.5 to  $24 \mu\text{m}$ . Most of these unresolved YSO sources had already been identified by Gouliermis et al. (2007) using observations in the range from 0.5 to

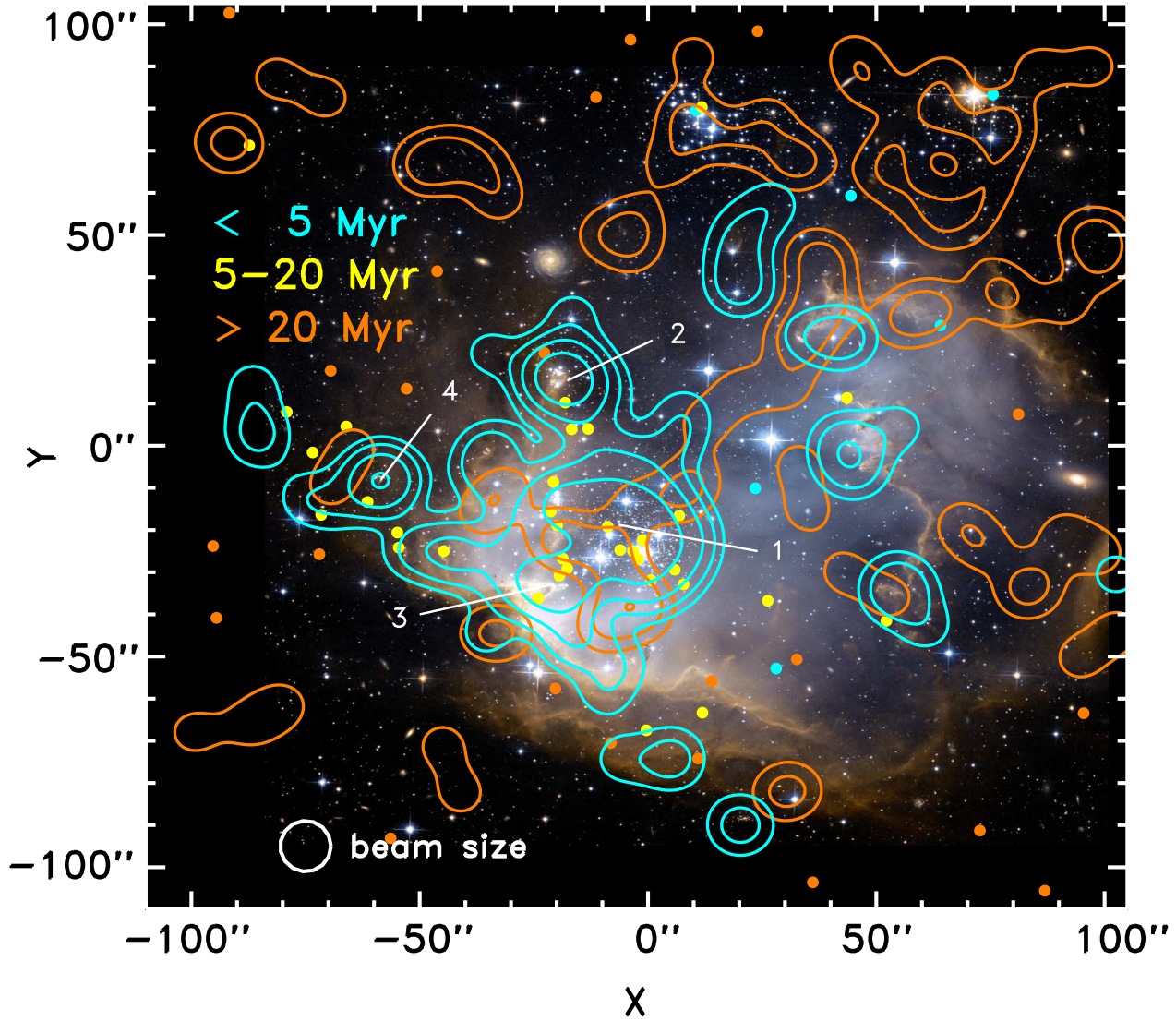


FIG. 8.— Contour plots showing the position and density distribution of PMS stars of different ages, as per the legend, overlaid on a true-colour image of the region. The lowest level corresponds to a density three times as high as the average density of PMS stars in the field. The step between contour levels is constant and corresponds to a factor of 2. Numbers 1 through 4 indicate the positions of the regions whose properties are shown in Table 1.

TABLE 1  
MEDIAN PROPERTIES OF THE STARS INSIDE REGIONS 1 – 4.

ID	IDG	X	Y	$N_{\text{PMS}}$	$m$ [ $M_{\odot}$ ]	$t$ [Myr]	$L(H\alpha)$ [ $L_{\odot}$ ]	$L^*$ [ $L_{\odot}$ ]
1	1	-7''	-20''	35	0.68	1.7	0.003	2.8
2	2	-18''	+15''	11	0.45	0.9	0.003	0.8
3	3	-22''	-33''	10	0.56	0.1	0.027	1.0
4	4	-58''	-8''	6	0.66	0.6	0.014	1.8

NOTE. — Table columns are as follows: ID number of the region; ID number as given by Gouliermis et al. (2012); X and Y coordinates in Figure 8; number of actively accreting PMS stars younger than 5 Myr in the region; their median mass, median age, median  $H\alpha$  luminosity, and median bolometric luminosity.

gressively triggered from the cluster centre outwards. This is inferred from the spatial distribution of the youngest YSOs (Stage I and I/II), which appear to lie farther from the cluster centre than older PMS stars, particularly along ridges located at the east-southeast and west of NGC 602 A.

In fact, what these observations actually reveal is an apparent systematic age difference between the OB and PMS stars near the cluster centre and the YSOs along the ridges, in the sense that the latter appear younger (by  $\sim 2$  Myr, according to Carlson et al. 2011). There are presently no measurements to tell whether the massive stars at the centre are responsible for the formation of the YSOs along the ridges. Therefore, the observations do not offer direct evidence of triggering, but rather indicate a case of sequential star formation: the episode at the centre appears to be already terminated (possibly caused

8  $\mu\text{m}$ . Both studies conclude that star formation is being pro-

by “fuel” exhaustion, as witnessed for instance by the lower level of the diffuse  $H\alpha$  emission there), while the one along the ridges is still ongoing.

Since the groups of unresolved YSOs studied by Carlson et al. (2011) are located in regions of higher nebulosity, along the ridges surrounding NGC 602 A, it is in principle possible that the reported age difference between them and the stars in NGC 602 A be only apparent and due to a higher extinction towards the ridges. Interestingly, also in our photometry most of the youngest PMS stars (those with an inferred isochronal age younger than 0.1 Myr) are located in regions of enhanced nebulosity, coinciding with the locations of the groups of unresolved YSOs of Carlson et al. (2011). While we have assumed the same extinction value for all stars in this region ( $A_V = 0.25$ ), as mentioned in Section 2, if the extinction towards the youngest PMS stars were about 2 mag higher, their ages would become fully compatible with those of the other young PMS objects at the cluster centre. To understand whether this is the case, we can look at the column density in these regions.

In the surroundings of NGC 602, an extinction of  $A_V = 1$  mag corresponds to a column density  $N(HI) = (7.4 \pm 1.2) \times 10^{21} \text{ cm}^{-2}$  (Gordon et al. 2003). The typical HI density in the heads of the gas pillars along the ridges is about  $1.5 \times 10^4 \text{ cm}^{-3}$ , corresponding to a column density of  $\sim 2 \times 10^{22} \text{ cm}^{-2}$  (Panagia & De Marchi, in preparation). This would in turn generate an extinction of order  $A_V \simeq 3$  towards the objects near the pillars, in good agreement with their observed colours if they are indeed PMS stars with an age similar to that of the objects in the cluster’s centre. Therefore, in principle, our youngest PMS stars and the unresolved YSOs of Carlson et al. (2011) could be highly reddened objects with ages of  $\sim 2$  Myr. On the other hand, some of the reddest PMS stars in the CMD do not coincide with regions of high nebulosity, and it is thus likely that they are intrinsically younger than the rest. The question, therefore, remains open as to whether the PMS stars along the ridges are systematically younger than those at the cluster centre. A spectroscopic investigation of the presence and intensity of Lithium absorption lines in these stars will be required to clarify the nature and intrinsic age of these objects.

In the meanwhile, we can set constraints on the relative ages of these young objects from their  $H\alpha$  luminosity  $L(H\alpha)$ . We list in Table 1 the values of  $L(H\alpha)$  of all PMS stars younger than 5 Myr located inside four sub-clusters, corresponding to local concentrations of young PMS stars indicated by the numbers 1 through 4 in Figure 8. Stars in regions 3 and 4 are typically redder in the CMD than those in regions 1 and 2, and comparison with isochrones results in a younger age. An indication that these stars are indeed intrinsically younger than those in regions 1 and 2 is provided by their  $L(H\alpha)$ , which is a factor of 5–10 higher. Interestingly, while the level of nebulosity is prominent in region 3, there is very little of it in region 4, further confirming that these latter stars are intrinsically very red and therefore intrinsically young.

An independent sign of the young ages of the PMS stars identified by the cyan contour lines in Figure 8 comes from X-ray observations. The distribution of our young PMS stars agrees rather well with the extended X-ray emission measured by Oskinova et al. (2013) in this field using *Chandra*. For ease of comparison, we show in Figure 9 the areas of extended X-ray emission by means of the contour levels (orange lines) obtained by Oskinova et al. (2013), together with an intensity

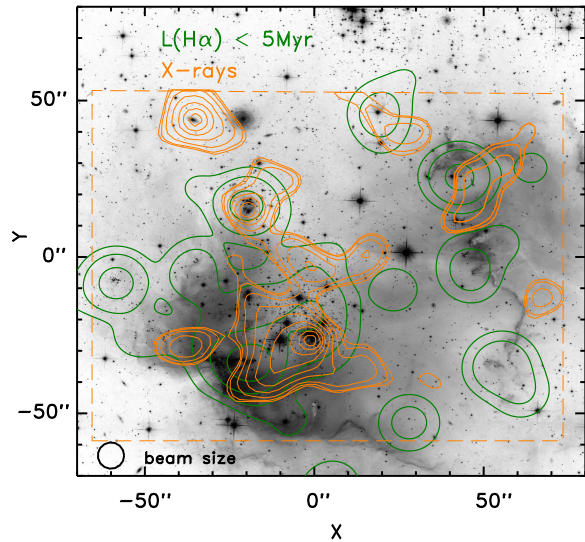


FIG. 9.— Same as Figure 8, but the underlying  $H\alpha$  image is shown in negative, on a grey scale. The cyan contours correspond to the  $H\alpha$  luminosity of PMS stars younger than 5 Myr, with the lowest level set to  $L(H\alpha) = 10^{-5} L_{\odot}$  and a constant logarithmic step of factor of 3. The orange contour lines are taken from Oskinova et al. (2013) and correspond to levels ranging from  $5 \times 10^{-4} \text{ cnt s}^{-1} \text{ arcmin}^{-2}$  to  $8 \times 10^{-4} \text{ cnt s}^{-1} \text{ arcmin}^{-2}$  on a square-root scale. The dashed lines define the *Chandra* field of view, while the prominent X-ray source near the top left corner is a background galaxy.

map (green lines) of the  $H\alpha$  luminosity from all our PMS stars younger than 5 Myr. The  $H\alpha$  intensity map differs slightly from the cyan contour lines of Figure 8, which represent the number density of PMS stars. The extent of the *Chandra* field of view is marked by the dashed lines. The negative image in the background is the one obtained in the  $H\alpha$  band.

At the distance of NGC 602, X-ray emission from individual PMS stars is too faint to be detected, but in general terms, there is an overall good match between the peaks of the X-ray and  $H\alpha$  maps, although in the detail some differences are present. For instance, in the central cluster the peak of the X-ray emission appears to coincide with the location of the most massive stars, whereas the peak of the  $H\alpha$  emission from low-mass stars is  $\sim 10''$  further north. This can be understood if, as Oskinova et al. (2013) point out, the diffuse X-ray emission at the cluster centre originates from (and is anyhow strongly affected by) a wind-blown bubble. In this case, the X-ray peak will be determined by the position of the massive objects.

Another difference concerns region 4 in Table 1, which is classified by Gouliermis et al. (2012) as a young cluster (also labelled 4 in their list) but that does not reveal diffuse X-ray emission. This apparent discrepancy, however, stems from the specific detection limit of the *Chandra* observations of Oskinova et al. (2013), namely  $L_X \simeq 10^{32} \text{ erg s}^{-1}$  (L. Oskinova, priv. comm.), which prevents clusters of smaller sizes to be detected above the noise. The study of the Orion Nebula Clusters conducted by Preibisch & Feigelson (2005) reveals typical values of  $L_X \simeq 3 \times 10^{30} \text{ erg s}^{-1}$  for  $\sim 1$  Myr old stars and masses similar to those in our sample ( $0.4 - 1 M_{\odot}$ ). If the same X-ray luminosity applies to stars in a lower metallicity environment such as NGC 602, only clusters with at least 10 – 15 young sources would be detectable in the observations of Oskinova et al. (2013). At older ages, the typical X-ray luminosity decreases (by a factor of  $\sim 5$  at an age of  $\sim 20$  Myr;

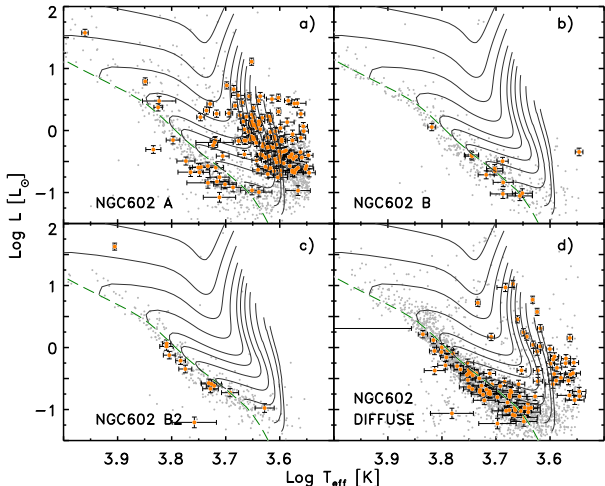


FIG. 10.— H–R diagrams for the various clusters in the field of NGC 602. Objects shown as thick dark dots (orange in the online version) are PMS stars as in previous figures (error bars on effective temperature and bolometric luminosity are also shown). Panel a) contains all stars within  $\sim 50''$  of the central NGC 602 A cluster, including regions 1–4 in Table 1. Panels b) and c) include all stars within  $\sim 25''$  of the clusters NGC 602 B and NGC 602 B2. Panel d) contains the diffuse population in the rest of the field. Evolutionary tracks are as in Figure 4, for masses of 0.45, 0.5, 0.6, 0.7, 0.8, 0.9, 1.0, 1.2, 1.5, 2.0, and  $3.0 M_{\odot}$  from bottom to top.

see Preibisch & Feigelson 2005), thereby making it even more difficult to detect these sources. Indeed, none of the regions in Figure 8 dominated by PMS stars older than 20 Myr, discussed in the following section, correspond to peaks in the *Chandra* X-ray map.

### 5.3. Older PMS stars

Older PMS stars, traced by the orange contours in Figure 8, mark the regions where star formation has been active in the recent past. Some of these objects are seen against regions where gas is still present, for example the regions of higher nebulosity in the immediate surroundings of the central cluster NGC 602 A and to the west of it. The fact that much younger PMS objects are also found in some of these regions indicates that there is still enough gas to sustain extended episodes of star formation, although this does not imply any triggering of star formation but rather a sequential process, in which multiple generations are born in the same location. In other regions, however, older PMS stars are not surrounded by younger PMS objects nor by nebulosity, suggesting that in those places star formation is no longer active. This is the case of the two small clusters, at the northern edge of the frame in Figure 8, respectively named by Cignoni et al. (2009) NGC 602 B (at  $X = +10''$ ,  $Y = +80''$ ) and NGC 602 B2 (at  $X = +70''$ ,  $Y = +70''$ ). The H–R diagrams of the stars within  $\sim 25''$  of their centres are compared in Figure 10 with those of the central cluster NGC 602 A (including regions 1–4 in Table 1) and with the diffuse population in the rest of the field.

Previous studies had assigned to NGC 602 B and NGC 602 B2 ages older than the stars of NGC 602 A, albeit with large uncertainties. Schmalzl et al. (2008) gave upper limits of respectively 180 Myr and 80 Myr to the ages of NGC 602 B and NGC 602 B2. These authors also note that, depending on how the brightest star in NGC 602 B is classified, its age too could be of order  $\sim 80$  Myr. Cignoni et al. (2009) compared the CMDs of the two clusters with isochrones based on FRANEC evolutionary tracks (Chieffi & Straniero 1989), showing that both are compatible with

ages in the range 15–150 Myr. The uncertainty, however, is still very large: these authors acknowledge that the age differences between these two clusters and the central NGC 602 A are only due to two stars evolved off the MS in NGC 602 B and NGC 602 B2. They conclude that, due to the paucity of stars, the ages of the two subclusters are practically indistinguishable from that of NGC 602 A.

On the other hand, the presence of a conspicuous number of older PMS stars still actively accreting, as shown in Figure 10, allows us to set much more stringent constraints on the relative ages of the two subclusters. We have derived the ages of these PMS objects using the PMS evolutionary tracks of the Pisa group (Tognelli et al. 2012) using a finer grid of models than the one shown in Figure 10, following the procedure explained in Section 4. We find average ages of, respectively,  $50 \pm 8$  Myr for NGC 602 B and  $47 \pm 7$  Myr for NGC 602 B2. Based on the quoted uncertainties and even including possible systematic errors in the PMS evolutionary tracks, we conclude that the two clusters are coeval and considerably older than the central cluster NGC 602 A.

A further indication that the two clusters have rather similar ages comes from the fraction of PMS stars along the MS, i.e. the fraction of objects that have already reached the MS but that were still accreting at the time of the observations (see Figure 10). For both clusters we find that this fraction is  $\sim 8\%$  in the magnitude range spanned by PMS stars ( $24 \leq V \leq 27$ ). Note that these values are lower limits to the actual fraction of PMS stars, because they only include objects with  $H\alpha$  excess emission at the  $4\sigma$  level or more at the time of the observations and because the objects without excess may also include a number of much older field stars, not related to these clusters. As mentioned before, the fraction of objects with  $H\alpha$  excess emission among stars younger than 5 Myr is about twice as large ( $\sim 15\%$ ), but that value too is a lower limit, since the region of the CMD where these objects fall can be populated by more massive and older objects subject to differential reddening. It is reassuring that the ratio of stars with and without  $H\alpha$  excess is larger for younger objects, as expected from stellar evolution, albeit not as large as the value of 28% found by De Marchi et al. (2011b) for the  $\sim 1$  Myr old PMS stars in NGC 346.

## 6. MASS ACCRETION RATE AND ITS EVOLUTION

The physical parameters derived in Section 4 allow us to determine the mass accretion rate of the PMS stars. The mass accretion rate  $\dot{M}_{\text{acc}}$  is related to the accretion luminosity  $L_{\text{acc}}$  via the free-fall equation, linking the luminosity released by the impact of the accretion flow with the rate of mass accretion, according to the relationship:

$$L_{\text{acc}} \simeq \frac{GM_* \dot{M}_{\text{acc}}}{R_*} \left(1 - \frac{R_*}{R_{\text{in}}}\right) \quad (6)$$

where  $G$  is the gravitational constant,  $M_*$  the mass of the star determined above,  $R_*$  its photospheric radius coming from its luminosity and effective temperature, and  $R_{\text{in}}$  the inner radius of the accretion disc. The value of  $R_{\text{in}}$  is rather uncertain and depends on how exactly the accretion disc is coupled with the magnetic field of the star. Following Gullbring et al. (1998), we adopt  $R_{\text{in}} = 5 R_*$  for all PMS objects and with this assumption we have all the parameters needed to determine  $\dot{M}_{\text{acc}}$ .

The median value of  $\dot{M}_{\text{acc}}$  that we derive is  $10^{-8} M_{\odot} \text{ yr}^{-1}$ , but the  $\dot{M}_{\text{acc}}$  distribution shows two clear peaks, at  $\sim 4.0 \times$

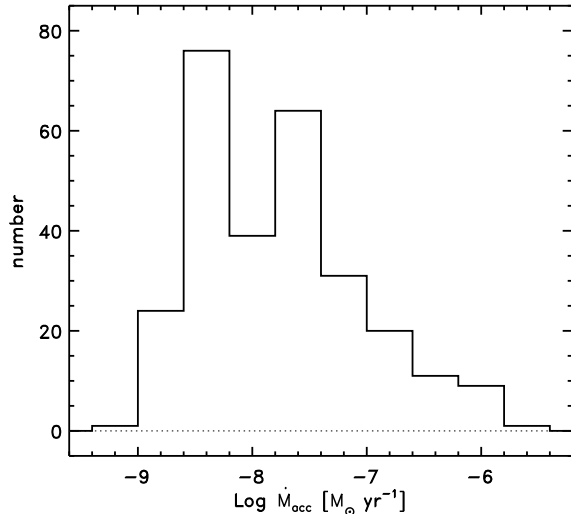


FIG. 11.— Distribution of the measured mass accretion rates.

$10^{-9} M_{\odot} \text{ yr}^{-1}$  and  $\sim 2.5 \times 10^{-8} M_{\odot} \text{ yr}^{-1}$ , suggesting the presence of two different populations in the field (see Figure 11). The separation between the two peaks is considerably larger than the observational uncertainties on  $\dot{M}_{\text{acc}}$ . Papers I and II provide an extensive discussion of the statistical and systematic uncertainties involved in determining the mass accretion rate with this method and on its basis we conclude that the combined statistical uncertainty on  $\dot{M}_{\text{acc}}$  for the stars in our field is 13%. Note that this is just the statistical uncertainty, but as extensively discussed in Papers I and II systematic uncertainties can dominate, particularly the conversion from  $L(H\alpha)$  to  $L_{\text{acc}}$ . If the uncertainty on the latter relation were as large as Dahm’s (2008) work suggests, it could possibly cause a systematic effect of up to a factor of 3 on the value of  $\dot{M}_{\text{acc}}$  that we obtain. However, as we explained in Paper II, this uncertainty cannot be as large as the 0.47 dex value suggested by an elementary fit to the data in the limited compilation of Dahm (2008), because it has to be intrinsically smaller than the  $\sim 0.25$  dex dispersion that we observe in NGC 346 (Paper II). This will also be visible for NGC 602 itself in Figure 13.

Nevertheless, neither statistical nor systematic uncertainties are able to explain the double peak in Figure 11. Its origin, however, becomes clearer when the measured  $\dot{M}_{\text{acc}}$  values are compared with the positions of the stars in the H–R diagram. In Figure 4, the size of the symbols corresponding to the PMS objects was set to be proportional to  $\dot{M}_{\text{acc}}$ , as per the legend in the figure. It is immediately apparent that younger objects have typically higher mass accretion rates than stars already approaching the MS, as expected from common wisdom about the theory of disc evolution.

The wide range of ages and masses covered by the PMS stars in our sample allows us to study in detail how the mass accretion rate varies with these parameters. To this end, we show in Figure 12 the variation of  $\dot{M}_{\text{acc}}$  as a function of stellar age. The PMS stars in NGC 602 are shown as dark diamonds (orange in the online version), with a symbol size proportional to their mass. Light grey diamonds in the same figure (pink in the online version) correspond to the PMS objects identified with the same method in NGC 346 in Paper II, also with a size proportional to their mass. The other symbols in the

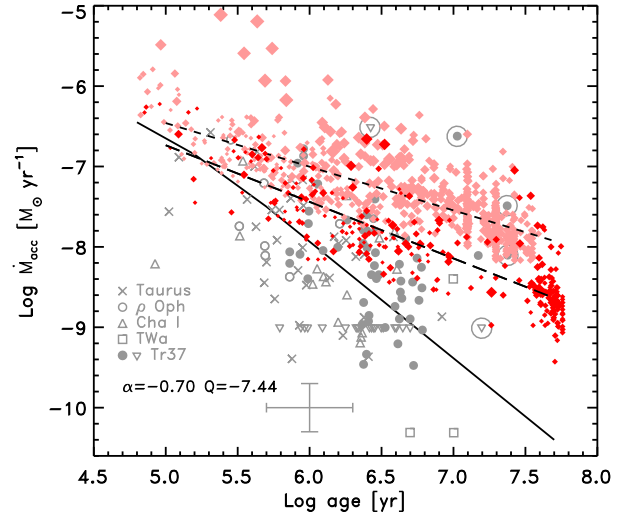


FIG. 12.— Derived mass accretion rates as a function of the age of the PMS stars. Dark diamonds (red in the online version) are for stars in NGC 602, whereas light grey diamonds (pink in the online version) are for the PMS objects in NGC 346. In both cases the size of the symbols is proportional to stellar mass. The long- and short-dashed lines are the best linear fits to the observed distributions in NGC 602 and NGC 346, respectively (the slope  $\alpha$  and intercept  $Q$  at 1 Myr are given for NGC 602). The other symbols, as per the legend, correspond to a sample of Galactic T-Tauri stars studied by Sicilia-Aguilar et al. (2006), with their typical uncertainty shown by the large cross at the bottom (the large circles around some of the symbols indicate dwarfs of spectral type G in the Trumpler 37 sample). Their distribution, in spite of the large scatter, is consistent with the models of viscous disc evolution of Hartmann et al. (1998) shown by the solid line.

figure (see legend) correspond to nearby T-Tauri stars in the sample of Sicilia–Aguilar et al. (2006) and are shown here for reference (the large circles around some of the symbols indicate dwarfs of spectral type G in the Trumpler 37 sample).

The long dashed line in Figure 12 represents the best fit to the observed distribution of mass accretion rates in NGC 602. Its slope ( $\alpha = -0.7$ ) is rather similar to the one measured in Paper II for stars of similar masses and ages in NGC 346 ( $\alpha = -0.55$ ), but the mass accretion rate is systematically lower in NGC 602 at all masses and ages. On the other hand, both slopes are considerably less steep than the  $\sim t^{-1.5}$  decline predicted by the models of Hartmann et al. (1998; see also Calvet et al. 2000; Muzerolle et al. 2000) for viscous disc evolution, represented here by the solid line, which reproduces rather well the trend of decreasing  $\dot{M}_{\text{acc}}$  with stellar age for low-mass Galactic T-Tauri stars as compiled by Sicilia–Aguilar et al. (2006). At face value, this discrepancy would seem to imply a different evolution of the mass accretion rate for PMS stars in the Galaxy and in the SMC. However, there are two conceptual problems with the type of comparison implied by Figure 12 that affect the conclusions that one can draw from it: (i) the masses of the individual objects must be taken explicitly into account; and (ii) the graph offers just a snapshot of the observed distribution of mass accretion rates and further assumptions are needed to infer from it an evolutionary path.

The first problem is easy to address, since the large size of our sample allows us to study the mass dependence of  $\dot{M}_{\text{acc}}$  in a robust way. In Papers I, II and III we found that the typical  $\dot{M}_{\text{acc}}$  of PMS stars in the LMC and SMC is systematically higher than for PMS stars of the same mass, independently of their age. To explore whether that is also the

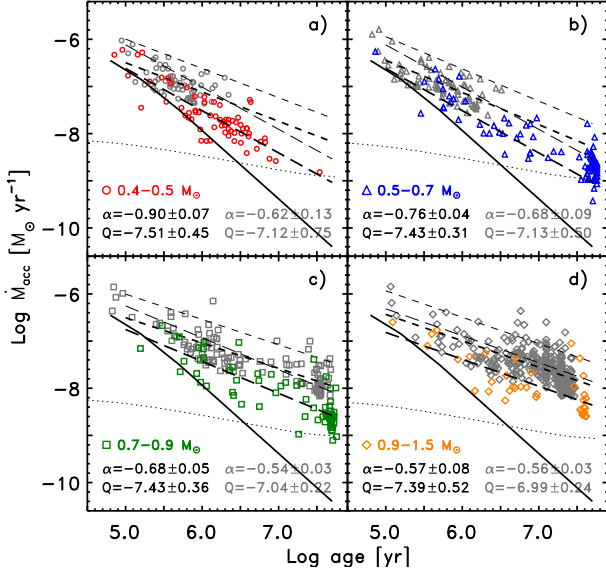


FIG. 13.— Same as Figure 12 but for stars in four mass groups, as indicated in each panel. We also provide the slope  $\alpha$  and intercept  $Q$  (at 1 Myr) of the best fits (thick long-dashed lines). NGC 346 data points and fit parameters are indicated in lighter grey, while the best linear fit is shown by the thick short-dashed lines. The thick solid line shows the models of Hartmann et al. (1998) for comparison. The dotted lines correspond to our  $L(H\alpha)$  detection limits and are different in each panel owing to the slightly different  $M/R$  values of each mass group.

case for NGC 602, in Figure 13 we split our sample in four roughly equally populated mass groups, namely  $0.4-0.5 M_{\odot}$ ,  $0.5-0.7 M_{\odot}$ ,  $0.7-0.9 M_{\odot}$  and  $0.9-1.5 M_{\odot}$ , and plot for each one separately the run of  $\dot{M}_{\text{acc}}$  as a function of age. The slope  $\alpha$  and intercept  $Q$  (at 1 Myr) of the best linear fit to the data (thick long-dashed lines), according to the relationship  $\log \dot{M}_{\text{acc}} = \alpha \times \log(\text{age}) + Q$  with the age in Myr, are given in each panel together with their uncertainties. The same quantities for NGC 346 are shown in light grey and the corresponding best fit is indicated by the thick short-dashed lines. As regards the slopes, the comparison shows that there is good agreement between the two clusters, although the absence of low-mass stars older than  $\sim 2$  Myr in NGC 346 makes the comparison difficult in Panel a).

A marked difference, however, exists between the slopes of our best fits and the models of Hartmann et al. (1998; solid lines). As already discussed in Papers II and III, our stringent requirements on the  $H\alpha$  excess emission ( $4\sigma$ ) and on the corresponding  $H\alpha$  equivalent width ( $10 \text{ \AA}$ ) do in practice set a lower limit to the  $H\alpha$  luminosity that we accept and thus to the  $\dot{M}_{\text{acc}}$  value at a given mass or age. On the other hand, comparing the observations with our  $4\sigma$  selection thresholds (dotted lines, independently calculated in each panel for the average  $M/R$  ratio of the stars in that mass group) shows that these effects, if present, are not important in the determination of the slopes. This is also confirmed by the fact that the upper envelopes to the observed distributions of all four mass groups appear to be fully consistent with the slopes of the best fit. This is shown by the thin long-dashed and short-dashed lines (respectively for NGC 602 and NGC 346), which represent the best-fitting line shifted vertically by 0.5 dex.

Since our sample is quite rich, we can perform a multivariate least-square fit to the observations to derive the simultaneous dependence of  $\dot{M}_{\text{acc}}$  on stellar mass and age. We assume

a relationship of the type:

$$\log \dot{M}_{\text{acc}} = a \times \log t + b \times \log m + c, \quad (7)$$

where  $t$  is the age in Myr,  $m$  the mass in solar units and  $c$  a constant, corresponding to the intercept at 1 Myr and  $1 M_{\odot}$  (note that  $c$  is similar to the parameter  $Q$  defined above, but it characterises the simultaneous fit on mass and age). The resulting best fit gives  $a = -0.72 \pm 0.02$ ,  $b = 0.94 \pm 0.14$  and  $c = -7.19 \pm 0.24$ . The dependence on age and mass are very similar to those found in Paper II for the PMS stars in NGC 346, namely  $a = -0.59 \pm 0.02$ ,  $b = 0.82 \pm 0.09$ , confirming the similarity already noticed in Figure 13. As already concluded in Paper II for NGC 346, using approximate values of  $a = -0.6$  and  $b = 1$  results in a fit with very small residuals also for NGC 602. The corresponding values of  $c$  are  $-7.0$  and  $-7.4$  respectively for NGC 346 and NGC 602, reflecting the fact that the value of  $\dot{M}_{\text{acc}}$  is systematically higher for PMS stars in NGC 346 than in NGC 602 at any given mass or age. This is also visible in Figure 13, where for all mass groups the mass accretion rate in NGC 346 is consistently  $\sim 2.5$  times higher than in NGC 602. This difference is meaningful because both samples are large and cover a wide and overlapping range of masses and ages.

As already mentioned, a similar effect had already been noticed in Papers I, II, and III when comparing the mass accretion rates in the Magellanic Clouds with those of Galactic stars of similar age. It was suggested in those works that the higher  $\dot{M}_{\text{acc}}$  values in the Magellanic Clouds could be favoured by their lower metallicity. As discussed in Paper III, the radiation pressure of the forming star is expected to be less strong on lower-metallicity disc material. Even though this might not be the dominant effect in the evolution of the disc, it will delay its dissipation, thereby keeping the accretion process active for a longer time. In general, a lower metallicity implies a lower opacity, temperature and viscosity for the disc, and thus a longer viscous time (e.g. Durisen et al. 2007). Therefore, low-metallicity stars can undergo significant accretion for a longer time than higher metallicity stars, in general agreement with our measurements. In this sense, one could explain the higher observed  $\dot{M}_{\text{acc}}$  values in NGC 346, since its metallicity is a factor of two lower than that of NGC 602, as mentioned in Section 4. The fact that the mass accretion rate values in NGC 602 are about a factor of 2.5 lower than those in NGC 346 at the same mass and age strongly suggests that the mass accretion rate is a decreasing function of the metallicity. We will address this dependence in more detail in a forthcoming paper (De Marchi et al., in preparation), in which we compare the mass accretion rate values in NGC 346 and NGC 602 with those of stars in other massive clusters in the Galaxy (NGC 3603; Beccari et al. 2010) and LMC (30 Dor; De Marchi et al. 2011c; Paper III).

In summary, our analysis indicates that the mass accretion rate scales with the age as roughly  $t^{-0.6}$ , with the first power of the mass and it decreases with increasing metallicity. However, as mentioned above, the evolution of  $\dot{M}_{\text{acc}}$  with time is derived from the comparison of the mass accretion rates of stars of different ages. Unless stars of all ages formed in similar conditions, the observed snapshot of  $\dot{M}_{\text{acc}}$  values may not provide direct information on the temporal evolution of  $\dot{M}_{\text{acc}}$  (see also Natta et al. 2006). In particular, differences in the density, angular momentum or metallicity of the molecular cloud as it evolves could result in different star formation

properties, leading to different time scales for the accretion process and the dissipation of the circumstellar discs.

Furthermore, since the fraction of stars undergoing active mass accretion decreases with time (see Paper II), an increasingly larger number of mildly- or non-accreting stars will fall below our detection threshold (i.e. the dashed lines in Figure 13), thereby resulting in a shallower slope of the  $\dot{M}_{\text{acc}}$  vs.  $t$  relationship at older ages for the least massive stars. On the other hand,  $\dot{M}_{\text{acc}}$  appears to scale similarly with age for different masses and in rather different environments such as NGC 602, NGC 346 and the SN 1987A field (see Figure 13 and Paper II). This suggests that density and metallicity do not affect the way in which  $\dot{M}_{\text{acc}}$  varies with time, but rather its instantaneous value. Indeed, the average value of  $\dot{M}_{\text{acc}}$  at 1 Myr at a specific mass, i.e. the parameter  $Q$  in Figure 13, is systematically higher at higher masses and for lower metallicity. As such, the parameter  $Q$  is less affected by the uncertainties on the actual dependence of  $\dot{M}_{\text{acc}}$  on the stellar age and can thus more effectively be used to study environmental differences of the mass accretion rate.

## 7. SUMMARY AND CONCLUSIONS

We have studied the properties of the stellar populations in the field of NGC 602 as observed with the ACS camera on board the HST (proposal nr. 10248, principal investigator A. Nota; see Carlson et al. 2007), using a self-consistent method that allows us to reliably identify PMS stars undergoing active mass accretion, regardless of their age. The method (see Papers I and II) combines broad-band  $V$  and  $I$  photometry with narrow-band  $H\alpha$  imaging to identify all stars with excess  $H\alpha$  emission and to derive their accretion luminosity  $L_{\text{acc}}$  and mass accretion rate  $\dot{M}_{\text{acc}}$ . This allows us to study how star formation and the accretion process have proceeded over time. The main results of this work can be summarised as follows.

1. We have performed PSF-fitting photometry on the exposures in the  $V$ ,  $I$  and  $H\alpha$  bands, covering a field of  $\sim 3.3 \times 3.3$  around the centre of NGC 602. From our photometry, we have selected all objects with a combined mean uncertainty in the  $V$  and  $I$  bands not exceeding 0.1 mag and a well defined magnitude in the  $H\alpha$  band, for a total of 5 500 sources.
2. The CMD derived in this way reveals a well defined MS, extending from  $V \simeq 16$  to  $V \simeq 28$ , a subgiants branch, and a rich population of young PMS stars, brighter and redder than MS objects. This variety of stellar populations, already discussed in a number of recent papers (e.g. Carlson et al. 2007; Cignoni et al. 2009), attests to a complex star formation history in NGC 602. Assuming a distance modulus of  $18.92 \pm 0.03$  and the canonical reddening value  $E(B-V) = 0.08$ , we find an excellent fit to the upper MS with the Padua isochrones (Fagotto et al. 1994; Marigo et al. 2008) for metallicity  $Z = 0.004$ . The same set of models applied to NGC 346, also in the SMC, indicate a lower metallicity for the latter cluster, namely  $Z = 0.002$  (Paper II).
3. Using the self-consistent method developed in Papers I and II, we have searched for stars with  $H\alpha$  excess emission above the  $4\sigma$  level with respect to the reference provided by normal stars in the same field. In this way

we have identified 296 bona-fide PMS stars by selecting objects with  $H\alpha$  equivalent width in excess of  $10 \text{ \AA}$ . Their median  $H\alpha$  luminosity is  $2 \times 10^{-3} L_{\odot}$ .

4. We have derived effective temperatures and luminosities for these objects by comparing the photometry to the stellar atmosphere models of Bessell et al. (1998). In turn, the masses and ages for 276 of these objects were obtained by comparing their luminosities and effective temperatures with the PMS evolutionary models of the Pisa group (Tognelli et al. 2012). We adopted the metallicity  $Z = 0.004$ , which is the value indicated by the comparatively young massive stars in the cluster. The masses of the 276 PMS stars range from  $0.4 M_{\odot}$  to  $2.5 M_{\odot}$ , with a median of  $\sim 0.7 M_{\odot}$ . As regards the ages, there is a clearly bimodal distribution, with about 1/2 of the objects younger than  $\sim 5$  Myr, about 1/3 older than  $\sim 30$  Myr, and 50 objects at intermediate ages. This bimodality is clearly visible in the H–R diagram, where the peaks of their distributions are separated in effective temperature by  $\sim 4$  times the width of the distributions. Since our age resolution is limited to a factor of  $\sim \sqrt{2}$ , stars older than  $\sim 30$  Myr may actually belong to distinct episodes.
5. Vigorous episodes of mass accretion separated by longer quiescent phases, like those proposed by Baraffe et al. (2009, 2010), can be excluded as the origin of this bimodal distribution in the H–R diagram, because such a mechanism would be unable to explain the remarkably different spatial distribution of younger and older PMS stars in this field.
6. PMS stars younger than  $\sim 5$  Myr are distributed in groups near the cluster centre, as well as along the gas ridges surrounding it, partly overlapping with regions where unresolved groups of YSOs have been detected in the mid-IR with *Spitzer*. The richest amongst these groups are also detected by *Chandra* as local peaks of the diffuse X-ray emission above the detection limit of  $L_X \simeq 10^{32} \text{ erg s}^{-1}$ , although none of our sources is individually resolved by *Chandra*. Conversely, except for a few objects near the cluster centre, the distribution of PMS stars older than  $\sim 20$  Myr does not overlap with that of younger PMS objects and a large fraction of older PMS stars are found in two clusters located  $\sim 100''$  north of the centre. The absence of YSOs and diffuse X-ray emission at these locations confirms that these are not of the same “generation” as younger PMS stars and are intrinsically older.
7. The relative locations of younger and older PMS stars do not imply a causal effect or triggering of one generation on the other. The observations only reveal distinct, and as such most likely unrelated generations of stars in the same field. We conclude that sequential star formation is present in this field, without any clear signs of triggering.
8. We set a lower limit to the star formation rate for the current ( $\sim 2$  Myr) burst of  $\sim 3 \times 10^{-5} M_{\odot} \text{ yr}^{-1}$ , while at  $\sim 20$  Myr it drops by a factor of 30 to  $\sim 10^{-6} M_{\odot} \text{ yr}^{-1}$ . Both values are necessarily lower limits, since they only account for the stars in the range  $0.4\text{--}2.5 M_{\odot}$  that were

undergoing active mass accretion at the time of the observations. Although at face value the current star formation episode seems stronger, the total integrated output of the two populations is comparable. Considering the  $\sqrt{2}$  uncertainty on relative ages in our analysis, if the fraction of PMS stars with H $\alpha$  excess decays exponentially with time, the episode or episodes occurring more than  $\sim 30$  Myr ago might have been even stronger than the current one.

9. We have derived the mass accretion rate  $\dot{M}_{\text{acc}}$  of all bona-fide PMS stars on the basis of their H $\alpha$  luminosity and the other physical parameters. The median value of  $\dot{M}_{\text{acc}}$  is  $10^{-8} M_{\odot} \text{ yr}^{-1}$ , but the distribution is clearly bimodal, with median  $\dot{M}_{\text{acc}}$  values of  $2.5 \times 10^{-8} M_{\odot} \text{ yr}^{-1}$  and  $4.0 \times 10^{-9} M_{\odot} \text{ yr}^{-1}$  respectively for PMS stars younger than 5 Myr and older than 20 Myr. These values are about a factor of 2.5 lower than those measured in NGC 346 for PMS stars of similar age.
10. Our rich sample of PMS stars and its spread in mass and age allow us to study the evolution of the mass accre-

tion rate as a function of stellar parameters. Like in the case of NGC 346 (see Paper II), a multivariate linear regression fit shows that  $\log \dot{M}_{\text{acc}} \simeq -0.6 \log t + \log m + c$ , where  $t$  is the age of the star,  $m$  its mass and  $c$  the mass accretion rate for unit mass at 1 Myr. The value of  $c$  is  $-7.4$  for NGC 602 and  $-7.0$  for NGC 346. The fact that the mass accretion rate values in NGC 602 are about a factor of 2.5 lower than those in NGC 346 at the same mass and age suggests that the mass accretion may be a decreasing function of the metallicity, as discussed in Paper III.

We are indebted to an anonymous referee, whose constructive criticism has helped us to improve the presentation of this work. GDM thanks Lidia Oskinova for useful discussions and Marco Meneghetti for his assistance with the colour figures. GB acknowledges funding from the European Community's Seventh Framework Programme (FP7/2007–2013) under grant agreement No 229517. NP acknowledges partial support by HST-NASA grants GO-11547.06A and GO-11653.12A, and STScI-DDRF grant D0001.82435.

## REFERENCES

- Alencar, S., Basri, G., Hartmann, L., Calvet, N. 2005, *A&A*, 440, 595  
 Antonucci, S., Nisini, B., Giannini, T., Lorenzetti, D. 2008, *A&A*, 479, 503  
 Baraffe, I., Chabrier, G., Gallardo, J. 2009, *ApJ*, 702, L27  
 Baraffe, I., Chabrier, G. 2010, *A&A*, 521, A44  
 Barentsen, G., Vink, J., Drew, J., et al. 2011, *MNRAS*, 415, 103  
 Battinelli, P., Demers, S. 1998, *AJ*, 115, 1472  
 Beccari, G., Spezzi, L., De Marchi, G., et al. 2010, *ApJ*, 720, 1108  
 Beccari, G., Bellazzini, M., Lardo, C., et al. 2013, *MNRAS*, 431, 1995  
 Beccari, G., De Marchi, G., Panagia, N., Pasquini, L. 2013, *A&A*, submitted  
 Bessell, M., Castelli, F., Plez, B. 1998, *A&A*, 333, 231  
 Bohlin, R. 2012, Instrument Science Report, ACS 2012-01, (Baltimore:STScI)  
 Bopp, B., Schmitz, M. 1978, *PASP*, 99, 531  
 Bopp, B., Talcott, J. 1978, *AJ*, 83, 12  
 Calvet, N., Hartmann, L., Strom, E. 2000, in "Protostars and Planets", eds V. Mannings, A. Boss, S. Russell (Tucson: University of Arizona Press), 377  
 Carlson, L., Sabbi, E., Sirianni, M., et al. 2007, *ApJ*, 665, L109  
 Carlson, L., Sewilo, M., Meixner, M., et al. 2011, *ApJ*, 730, 78  
 Chieffi, A., Straniero, O. 1989, *ApJS*, 71, 47  
 Cignoni, M., Sabbi, E., Nota, A., et al. 2009, *AJ*, 137, 3668  
 Dahm, S. 2008, *AJ*, 136, 521  
 Da Rio, N., Robberto, M. 2012, *AJ*, 144, 176  
 Degl'Innocenti, S., Prada Moroni, P.G., Marconi, M., Ruoppo, A. 2008, *Ap&SS*, 316, 25  
 De Marchi, G., Panagia, N., Romaniello, M. 2010, *ApJ*, 715, 1 (Paper I)  
 De Marchi, G., Panagia, N., Romaniello, M., et al. 2011a, *ApJ*, 740, 11 (Paper II)  
 De Marchi, G., Panagia, N., Sabbi, E. 2011b, *ApJ*, 740, 10  
 De Marchi, G., Paresce, F., Panagia, N., et al. 2011c, *ApJ*, 739, 27  
 Downes, R., Webbink, R., Shara, M., et al. 2005, *JAD*, 11, 2  
 Durisen, R., Boss, A., Mayer, L., et al. 2007, *Protostars and Planets V*, 607  
 Fagotto, F., Bressan, A., Bertelli, G., Chiosi, C. 1994, *A&AS*, 105, 29  
 Fedele, D., van den Ancker, M., Henning, T., Jayawardhana, R., Oliveira, J. 2010, *A&A*, 510, A72  
 Fernandez, M., Ortiz, E., Eiroa, C., Miranda, L. 1995, *A&AS*, 114, 439  
 Gardner, J. P., Mather, J. C., Clampin, M., et al. 2006, *SSRv*, 123, 485  
 Gordon, K., Clayton, G., Misselt, K., Landolt, A., Wolff, M. 2003, *ApJ*, 594, 279  
 Gouliermis, D., Quanz, S., Henning, T. 2007, *ApJ*, 665, 306  
 Gouliermis, D., Schmeja, S., Dolphin, A., et al. 2012, *ApJ*, 748, 64  
 Hartmann, L., Calvet, P., Gullbring, E., D'Alessio, P. 1998, *ApJ*, 495, 385  
 Heinke, C., Grindlay, J., Edmonds, P., et al. 2005, *ApJ*, 625, 796  
 Henize, K. 1956, *ApJS*, 2, 315  
 Hennekerper, E., Gouliermis, D., Henning, T., Brandner, W., Dolphin, A. 2008, *ApJ*, 672, 914  
 Hilditch, R., Howarth, I., Harries, T. 2005, *MNRAS*, 357, 304  
 Hutchings, J., Thompson, I., Cartledge, S., Pazder, J. 1991, *AJ*, 101, 933  
 Ingleby, L., Calvet, N., Herczeg, G., et al. 2013, *ApJ*, 767, 112  
 Keller, S. C., Wood, P. R. 2006, *ApJ*, 642, 834  
 Lee, J.-K., Rolleston, W., Dufton, P., Ryans, R. 2005, *A&A*, 429, 1025  
 Maybhathe, A., et al. 2010, "ACS Instrument Handbook", Version 10.0 (Baltimore: STScI)  
 Marigo, P., Girardi, L., Bressan, A., Groenewegen, M., Silva, L., Granato, G. 2008, *A&A*, 482, 883  
 Massey, P., Waterhouse, E., DeGioia-Eastwood, K. 2000, *AJ*, 119, 2214  
 Muzerolle, J., Calvet, N., Briceño, C., Hartmann, L., Hillenbrand, L. 2000, *ApJ*, 535, L47  
 Muzerolle, J., Calvet, N., Hartmann, L., 1998, *ApJ*, 492, 743  
 Natta, A., Testi, L., Randich, S. 2006, *A&A*, 452, 245  
 Nigra, L., Gallagher, J., Smith, L. et al. 2008, *PASP*, 120, 972  
 Nisini, B., Antonucci, S., Giannini, T., Lorenzetti, D. 2005, *A&A*, 429, 543  
 Panagia, N., Romaniello, M., Scuderi, S., Kirshner, R. 2000, *ApJ*, 539, 197  
 Oskinova, L. M., Sun, W., Evans, C. J., and 11 colleagues 2013, *ApJ*, 765, 73  
 Parker, Q., Phillipps, S., Pierce, M., et al. 2005, *MNRAS*, 362, 689  
 Perez-Montero, E., Diaz, A. 2005, *MNRAS*, 361, 1063  
 Preibisch, T., Feigelson, E. D. 2005, *ApJS*, 160, 390  
 Pretorius, M., Knigge, C. 2008, *MNRAS*, 385, 1471  
 Pretorius, M., Knigge, C. 2013, *MNRAS*, 432, 570  
 Rolleston, W., Dufton, P., McErlean, N., Venn, K. 1999, *A&A*, 348, 728  
 Romaniello, M. 1998, PhD thesis, Scuola Normale Superiore, Pisa, Italy  
 Romaniello, M., Panagia, N., Scuderi, S., Kirshner, R. 2002 *AJ*, 123, 915  
 Romaniello, M., Robberto, M., Panagia, N. 2004, *ApJ*, 608, 220  
 Russell, S. C., Dopita, M. A. 1992, *ApJ*, 384, 508  
 Schmalzl, M., Gouliermis, D., Dolphin, A., Henning, T. 2008, *ApJ*, 681, 290  
 Scuderi, S., Panagia, N., Gilmozzi, R., Challis, P., Kirshner, R. 1996, *ApJ*, 465, 956  
 Sicilia-Aguilar, A., Hartmann, L., Furesz, G., Henning, T., Dullemond, C., Brandner, W. 2006, *AJ*, 132, 2135  
 Sirianni, M., Jee, M., Benitez, N., et al. 2005, *PASP*, 117, 1049  
 Smith, K., Lewis, G., Bonnell, I., Bunclark, P., Emerson, J. 1999, *MNRAS*, 304, 367  
 Spezzi, L., De Marchi, G., Panagia, N., Sicilia-Aguilar, A., Ercolano, B. 2012, *MNRAS*, 421, 78 (Paper III)  
 Staveley-Smith, L., Sault, R., Hatzidimitriou, D., Kesteven, M., McConnell, D. 1997, *MNRAS*, 289, 225  
 Stetson, P. 1987, *PASP*, 99, 191  
 Stetson, P., Harris, W. 1988, *AJ*, 96, 909  
 Stetson, P. 1994, *PASP*, 106, 250  
 Tognelli, E., Degl'Innocenti, S., Prada Moroni, P. G. 2012, *A&A*, 548, A41  
 Valenti, J., Basri, G., Johns, C. 1993, *AJ*, 106, 2024  
 Warner, B. 1995, *Cataclysmic Variable Stars* (Cambridge: Cambridge University Press)  
 White, R., Basri, G. 2003, *ApJ*, 582, 1109